TRANSITION METAL SUBSTITUTED TITANATES AND NIOBATES : SYNTHESIS, CHARACTERIZATION AND PHOTOCATALYTIC ACTIVITY

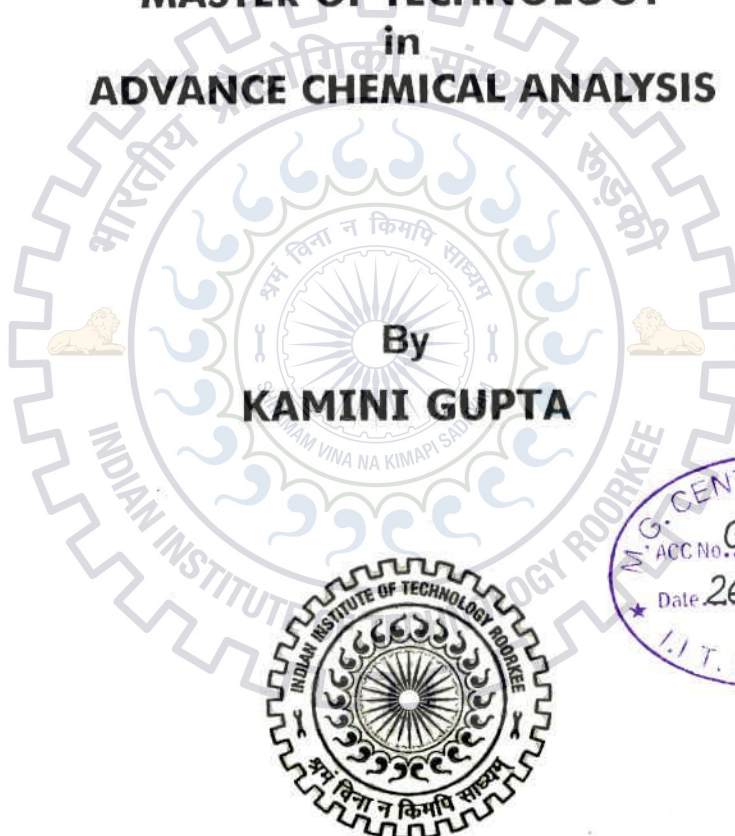## A DISSERTATION

Submitted in partial fulfillment of the
requirements for the award of the degree
of
MASTER OF TECHNOLOGY
in
ADVANCE CHEMICAL ANALYSIS

By

KAMINI GUPTA

**DEPARTMENT OF CHEMISTRY
INDIAN INSTITUTE OF TECHNOLOGY ROORKEE
ROORKEE -247 667 (INDIA)
JUNE, 2013**

CANDIDATE'S DECLARATION

I, hereby, declare that the work presented in this dissertation entitled **"TRANSITION METAL SUBSTITUTED TITANATES AND NIOBATES: SYNTHESIS, CHARACTERIZATION AND PHOTOCATALYTIC ACTIVITY"** in partial fulfillment of the requirements for the award of the degree of **Master of Technology** in **"Advanced Chemical Analysis"** submitted in the **Department of Chemistry** at **Indian Institute of Technology Roorkee**, is an authentic record of the work carried out by me during the period August 2012 to June 2013, under the guidance of **Dr. Tapas Kumar Mandal**, Assistant Professor, Department of Chemistry, Indian Institute of Technology Roorkee, Roorkee.

The matter presented in this dissertation work has not been submitted by me for the award of any degree of this or any other Institute/ University. In keeping with the general practice of reporting scientific observation, due acknowledgement has been made wherever the work described is based on the findings of other investigators.

Date: June, 2013

Place: Roorkee

(Kamini Gupta)

i

CERTIFICATE

This is to certify that the above statement made by the candidate is correct to the best of my knowledge.
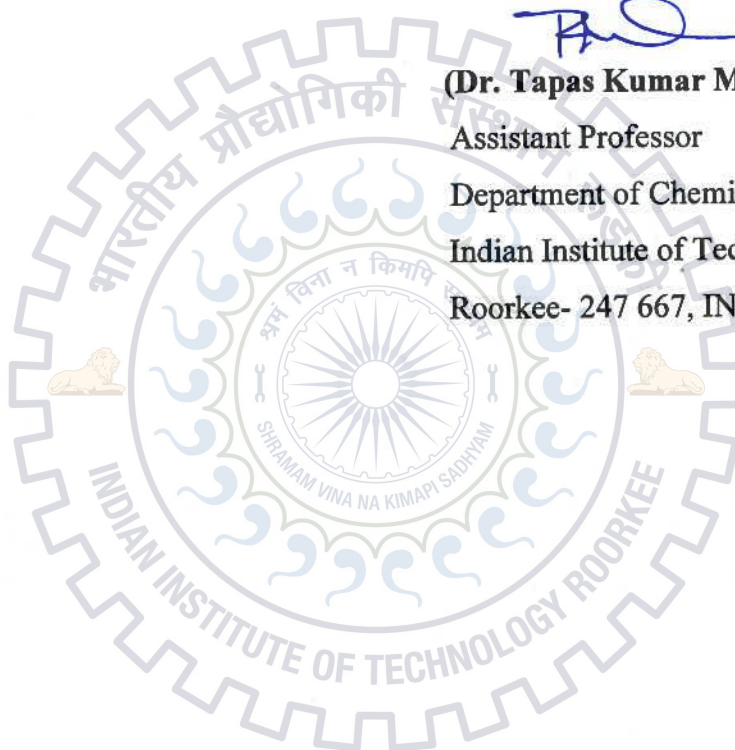
(Dr. Tapas Kumar Mandal)

Assistant Professor

Department of Chemistry

Indian Institute of Technology Roorkee

Roorkee- 247 667, INDIA

Acknowledgement

Finally, I must thank all those whom I have failed to state here but have helped in various ways during the course of my research.

(KAMINI GUPTA)

CONTENTS

ABSTRACT

New transition metal-substituted perovskite titanates, $Pb_{1-x}La_xTi_{1-x/2}M_{x/2}O_3$ (M = Fe, Co, Mn) and Dion-Jacobson type layered perovskite niobates, $KCa_{2-x}La_xNb_{3-x/2}M_{x/2}O_{10}$ (M = Fe, Mn, Co) have been synthesized. The compounds are characterized by Powder X-ray Diffraction (PXD), Field Emission Scanning Electron Microscopy (FE-SEM), Energy Dispersive X-ray (EDX) analysis and UV-Visible Diffuse Reflectance Spectroscopy (UV-Vis DRS). Photocatalytic activity of the Fe-members of both the series of compounds has been explored by way of Methylene Blue degradation under natural sunlight. The details of these investigations are presented in the dissertation.
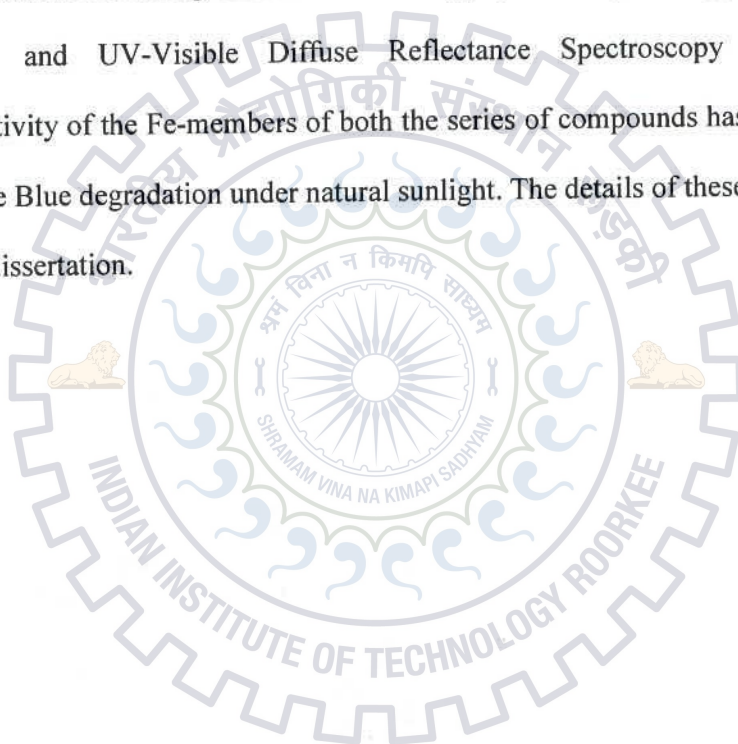
CHAPTER-I

Introduction

Energy generation and environmental pollution are two major problems in present day scenario as well as in upcoming future time. Semiconductor photocatalysis seems a promising solution for both the problems. The discovery of Fujishima and Honda in 1972 that water can get splitted photo-electrochemically into its constituents H_2 and O_2 under UV light on the surface of TiO_2 and Pt electrode was a breakthrough in the area of photocatalysis [1]. Later on extensive works have been carried out in the field of heterogeneous photocatalysis [2-9].

In recent years, a lot of research was devoted towards environmental application of heterogeneous photocatalysis [10, 11]. Wastewater treatment, indoor air purification, dye degradation etc. are some example of its environmental applications. However, most of the photocatalysts developed for this purpose are limited to only ultraviolet light. Efforts are being made to develop photocatalysts that are active in the visible region, so that natural sunlight, which is available free of cost, abundant and non-exhaustible, can be utilized [12-21].

Semiconductor particles act as heterogeneous photocatalysts for environmentally obstinate pollutants. Advanced oxidation process (AOP) is a relatively new technique which is used for purification of water [22]. In AOP, complete mineralization of pollutants or its conversion into less reactive species occurs by oxidation processes assisted mainly by hydroxyl radicals. There are other traditional wastewater treatment techniques, for example, activated carbon adsorption, chemical oxidation, biological treatment etc. but they have limitations.

1

Likewise, in activated carbon adsorption method, complete degradation of pollutants does not take place since it involves only phase transfer without any decomposition. Similarly, chemical oxidation is also not a very efficient process. Moreover, it is costly and complete mineralization of pollutants does not take place. In biological treatment, the main drawback is its slow reaction rate. Disposal of sludge, maintaining the pH and temperature are among the major problems associated with the biological treatment processes.

Photocatalysis is an example of AOP and it can be used for removal of pollutant in relatively lower concentration ($\mu g/l$) from water and air. Complete photocatalytic degradation of pollutants is indicated by the formation CO_2, H_2O and inorganic mineral salts, which are mostly the end products of degradation processes [22, 23]. Photocatalytic mineralization of various pesticides using TiO_2, under both artificial and solar light, has been reported in the literature [24].

Apart from TiO_2, several other oxides and sulphide photocatalysts, such as, CdS, ZnS, ZnO, SnO_2, WO_3, Nb_2O5 and $LnTaO_4$ are reported in the literature [6, 8, 25-27]. In semiconductor photocatalysis, TiO_2 is one of the most studied materials, since it is stable, non-toxic, cheap and readily available. TiO_2 is usually found in three types of polymorphic forms, namely, rutile, anatase, and brookite. Among them, rutile is the most stable form of TiO_2. In all three forms, titanium (Ti^{4+}) is coordinated with six oxygens (O^{2-}) forming TiO_6 octahedra. However, their interconnections via two (rutile), three (brookite) or four (anatase) common edges gave rise to slight variations in their band gaps. While the band gap of rutile was about 3.0 eV that of brookite and anatase were close to 3.2 eV. Interestingly, one of the first environmental remediation applications of TiO_2 was reported by Frank and Bard way back in 1977 for the reduction of CN^- in water [28].

When a semiconductor photocatalyst material interacts with light of sufficient energy (i.e., energy greater than its band gap energy), it produces reactive oxidising species (ROS). In semiconductor photocatalysis, when light energy greater than band gap energy is fallen on a semiconductor, electrons from the valence band (VB) get excited to the conduction band (CB), thereby, creates a hole in the VB and electron in the CB. This can be represented by following equation.

$$TiO_2 \quad + \quad hv \quad \rightarrow \quad \underset{\text{(electron in CB)}}{e^-} \quad + \quad \underset{\text{(hole in VB)}}{h^+}$$
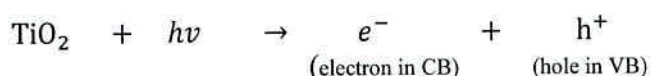
Charge carriers generated by this photoexcitation can either form Ti^{3+} and O^- defect sites in the TiO_2 lattice, recombine [29] or migrate to the catalyst surface and initiate redox reactions with the adsorbates. Positive holes can oxidise hydroxide ion (OH^-) and water at the surface and produce hydroxyl radicals ($^\cdot OH$). Hydroxyl radicals are powerful oxidant and it can oxidize organic species into CO_2, H_2O and mineralized salts. Reaction of hydroxyl radical can be represented as follows:

$$^\cdot OH + \text{organic species} \rightarrow CO_2 + H_2O$$

EPR studies suggest that hydroxyl radical are active oxidising species in photocatalytic degradation of organics on TiO_2, be it is free or surface bound [30].

Recombination is a process of returning back of the exited electron to the valence band without reacting with the adsorbed species. This process reduces the overall quantum efficiency of semiconductor photocatalysts. Recombination can occur either on the surface or in the bulk. Impurity and defects in semiconductor particles promote recombination process and ultimately affect the efficiency of photocatalyst. Since TiO_2 is active only under UV light and the major part

3

of solar radiation is visible light so for photocatalytic applications involving solar radiation band gap engineering of TiO_2 and other UV active photocatalysts are important.

In our attempt to engineer the band gap of oxide materials, we have chosen UV active three dimensional and layered perovskites and used transition metal-substitution as a strategy to modify their band gap. Perovskite oxides are represented by the general formula, ABO_3 [31]. The structure is formed by the corner shared octahedral framework of B-cation. The A cation can be rare earth, alkaline earth or other large ions, such as, Pb^{2+} and Bi^{3+} that fits in the dodecahedral site of the framework. The B-cations are mostly transition metals of be 3d, 4d or 5d series with both d^n (n = 1-9) or d^0 configuration. For the description of perovskite structures, Goldschmidt had introduced a tolerance factor known as 'Goldschmidt tolerance factor', t and is given by the expression,

$$t = \frac{rA + rO}{\sqrt{2}(rB + rO)}$$

Where, r_A, r_B and r_O are ionic radii of A, B and O, respectively. If t values are in between 0.8 to 1.0, perovskite structure gets stabilized. For $t = 1$, an ideal perovskite structure forms with no distortions. However, the structure distorts from an ideal perovskite when the value of t deviates from 1.0 [31]. Figure 1.1 shows an ideal perovskite structure.
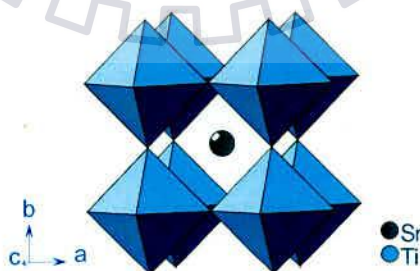

Figure 1.1: An ideal perovskite structure of SrTiO$_3$.

4

Perovskite structure can tolerate significant amount of partial substitution of metals at both the A and B sites and non-stoichiometries while maintaining the perovskite structure. Metal ion having different valences can replace both A and B atoms. Since perovskites can form variety of structure and composition this is an important research area in the field of solid state chemistry, physics, advance materials and catalysis.

Due to the compositional and structural flexibility of perovskites, several perovskite derived structures are possible. For example, the intergrowth of perovskite and other structures gives rise to a series of layered perovskites. Most common layered perovskites are the Aurivillius phases [32], the Ruddlesden-Popper (RP) [33] and the Dion-Jacobson (DJ) [34] phases. All the three series of layered perovskites contain common two dimensional perovskite sheets of composition $[A_{n-1}B_nO_{3n+1}]$, which are interleaved by $[Bi_2O_2]^{2+}$ units in Aurivillius, two alkali/alkaline earth cations in the RP and one alkali/alkaline earth cations in the DJ series. The DJ series can be represented by the general formula, $A'[A_{n-1}B_nO_{3n+1}]$ (where n is number of perovskite block). Figure 1.2 shows the structure of a representative n = 3 member of the DJ series, $CsCa_2Nb_3O_{10}$. The structure can be visualized as an intergrowth of perovskite and rock salt structure. The interest in DJ phase arises from reports of visible light driven photocatalytic activity in many of its member compounds [6, 7, 12, 13].

Titanates, niobates and tantalates having d^0 electronic configuration for the transition metal and with a three dimensional perovskite or layered perovskite structure show photocatalytic property mostly under UV-radiation [6, 7]. Doping of small amount of acceptor in $KTaO_3$ which is a Ta based perovskite, increased photodecomposition of water reported by Ishihara et al. [35]. $LaTiO_2N$, a perovskite oxynitride prepared by solid state reaction shows water splitting reaction under visible light [36]. $CeCo_xTi_{1-x}O_{3+\delta}$ perovskite type photocatalysts
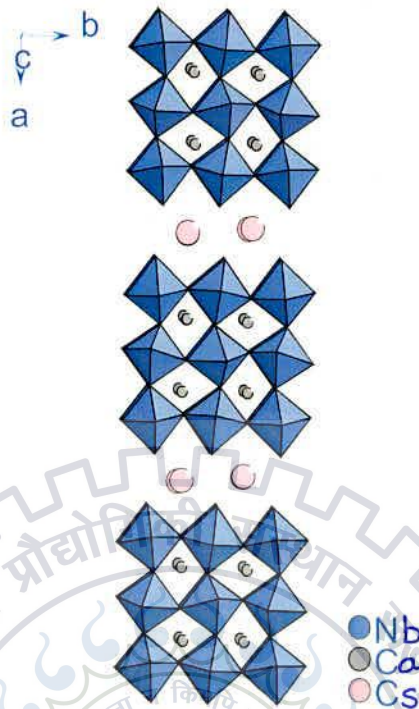
Figure 1.2: Dion-Jacobson layered perovskite structure of $CsCa_2Nb_3O_{10}$.

prepared by sol-gel method show photocatalytic activity under visible light [37]. In the recent past, an efficient photocatalytic decomposition of acetaldehyde was reported over a perovskite solid solution photocatalyst, $(Ag_{0.75}Sr_{0.25})(Nb_{0.75}Ti_{0.25})O_3$ [17]. The compound is having a band gap of ~ 2.8 eV and a visible light active photocatalyst. Although its parent perovskite, $AgNbO_3$ has a band gap in the visible, however, it shows only poor visible-light activity. This higher activity is attributed to a better charge carrier transportation due to favourable VB and CB states made up of Ag-$4d$+O-$2p$ and Ti-$3d$+Nb-$4d$ hybridized orbitals, respectively [17]. Recently, a red metallic oxide photocatalyst, $Sr_{1-x}NbO_3$, an A-site deficient cubic perovskite, was discovered. It

is shown to photocatalyse the oxidation methylene blue and oxidation and reduction of water in presence of sacrificial elements [38].

$KCa_2Nb_3O_{10}$ is a typical example of the DJ family. In layered perovskite type niobate, a variety of derivatives can be developed by substituting perovskite A and B site metals. It is reported that $RbPb_2Nb_3O_{10}$, where Pb is incorporated in the perovskite A site, shows increased photocatalytic activity towards H_2 evolution from aqueous methanol solution under visible light irradiation as compared to its protonated analogue [12]. The synthesis of this compound was initially reported by Subramanian *et al.* [39]. $PbBi_2Nb_2O_9$ is another single phase layered perovskite oxide, having an Aurivillius type structure, is an efficient photocatalyst ($E_g = 2.88$ eV) for the degradation of isopropyl alcohol to CO_2 [13]. Due to its single phase nature, the compound it is highly stable and do not dissolve even after 100 h of photocatalytic water decomposition reaction.

$A'_{1-x}Na_xCa_2Ta_3O_{10} \cdot nH_2O$ where (A' = K and Li) are examples of hydrated phase of DJ type layered perovskite. The series results by replacement of Na in the parent $KCa_2Ta_3O_{10}$. The compounds show interlayer hydration, which increases the photocatalytic activity under the UV radiation for splitting of water [40]. Recently, wide band gap tunability in complex transition metal oxides has been demonstrated by way of site specific substitution in a layered ferroelectric bismuth titanate. This has opened up an enormous possibility of controlling the band gap in complex oxides [41].

In the present study, we have undertaken the synthesis and characterization of transition metal-substituted titanate and niobates based on perovskite and Dion-Jacobson type layered perovskite structure, respectively. The syntheses of new compounds were carried out by solid

7

state reactions of high purity metal oxides/carbonates/oxalates. The compounds were characterized by Powder X-ray Diffraction (PXD), Field Emission Scanning Electron Microscopy (FE-SEM), Energy Dispersive Analysis by X-Rays (EDAX), UV-Visible Diffuse Reflectance Spectroscopy (UV-Vis DRS) and SQUID magnetometry. Photocatalytic activities of selected compounds were studied by way of dye degradation under visible light irradiation. The details of the investigations are described in the subsequent chapters.

CHAPTER-II

Experimental Methods

2.1 Synthesis

Solid state reaction or the ceramic method was mainly used for the preparation of transition metal-substituted perovskite and layered perovskite oxides. The starting materials, metal oxides and carbonates used for solid state reactions, were high purity (> 99%) chemicals purchased from Sigma/Sigma-Aldrich and used directly without any further purification. Transition metal oxalates used in the reactions were prepared in the laboratory by a solution precipitation method. For this purpose, nearly equimolar quantities of transition metal nitrates/chlorides and oxalic acid (in 10 mole% excess) were dissolved in minimum volumes of distilled water in two separate beakers. One of the so prepared solutions was then poured into the other and mixed thoroughly with vigorous stirring. Transition metal oxalates, $MC_2O_4 \cdot 2H_2O$ (M = Mn, Fe, Co), for different transition metals were precipitated from the solution with slightly different delay times. The precipitates were settled, filtered with Whatman 42, washed thoroughly with distilled water and dried in a hot air oven at 70 °C. The oxalates thus prepared were checked for purity by powder X-ray diffraction (PXD) (see next section) prior to use.

Transition metal-substituted perovskite titanates and layered perovskites niobates were prepared by reactions of alkali/alkaline earth metal carbonates, lead/lanthanum/titanium/niobium oxides and transition metal oxalates. In a typical solid state reaction, stoichiometric quantities of

9

oxides, carbonates and oxalates were taken in an agate mortar and ground thoroughly for nearly an hour. The ground mixture was placed into a high quality (> 99.7 %) alumina boat and was kept in a muffle furnace at desired temperatures for heating. The reaction mixtures were ground thoroughly at each and every intermittent stage during the entire course of the reaction. Reaction conditions for the successful synthesis of a compound were worked out by trial and error method. For this, reaction mixtures were heated at different temperatures and for various durations. Through PXD analyses, phase formation and purity was monitored and reaction conditions were standardized.

2.2 Characterization

2.2.1 Powder X-ray diffraction (PXD)

Powder X-ray diffraction (PXD) measurements were carried out using a Bruker AXS D8 Advance diffractometer operating at 40 kV and 30 mA and using a graphite monochromatized CuK_α radiation (λ = 1.5406 Å). In typical experiments, loose powders were spread over a flat plate and the data were collected in the Bragg-Brentano geometry within an angular range of 5-90°.

The diffraction data of compounds were analyzed by comparing the observed data with standard diffraction data files (JCPDS) available in the ICDD database. The unit cell parameters of the newly synthesized compounds were determined by least-squares refinement of the observed reflections using the PROSZKI program [42]. XRD pattern simulations were carried out using the software 'Powder Cell 2.4' [43]. The structural data required for the pattern simulation are space group, lattice parameters, atom positions, site occupancy and thermal parameters. The simulations of powder patterns were performed based on a model crystal

10

structure and suitably adjusting the atomic position and occupancy parameters relating to the compound composition. Thermal parameters were used as reported in the model structure.

2.2.2 UV-Visible Diffuse Reflectance Spectroscopy (UV-Vis DRS)

The UV-visible spectra in the diffuse reflectance mode for solid samples were recorded using a Shimadzu UV-2450 UV-Vis spectrophotometer within the wavelength range of 200-800 nm. For this purpose, $BaSO_4$ was used as a reference material for baseline correction. In a typical experiment, sample and $BaSO_4$ (1:100 ratio) were taken in a pestle and mortar and mixed thoroughly for about 5-10 minutes and the powder was pressed into a pellet and the data were recorded in the diffuse reflectance mode.

The approach used for describing the interaction of light with a diffuse media was the Kubelka-Munk theory. The Kubelka-Munk function is generally used for the analysis of diffuse reflectance spectra obtained from weakly absorbing samples and is given by equation (2.1):

$$F(R) = \frac{(1-R)^2}{2R} = \frac{k}{s} \qquad (2.1)$$

where $F(R)$ is the Kubelka-Munk function, R is diffuse reflectance, k is the absorption co-efficient and s is scattaring coefficient. The band gap were estimated by Sapiro's method [44, 45] and using the following equation (2.2):

$$\text{Band gap (eV)} = \frac{1242.375}{\lambda\ in\ nm} \qquad (2.2)$$

2.2.3 Field Emission Scanning Electron Microscopy (FE-SEM)

Morphology and elemental percentages were studied using a Quanta 200F FEI Netherland instrument's FE-SEM operated at 20 kV. The images were taken at a working distance (WD) of ~ 10.5 nm at magnifications of 5000×, 10000×, 20000× and 30000×.

The samples were prepared by spreading fine powders over a carbon tape pasted on a metal stub and coating with a thin layer of Au for electrical conductivity. The elemental percentages of samples were determined by Energy Dispersive X-ray Analysis (EDXA). The particle morphologies were seen at different places of the sample for homogeneity analysis. With EDAX, both spot and area analysis were carried out to know elemental compositions in many regions of the sample.

In a conventional SEM analysis, sputter gold coated sample target is bombarded with heavy gas atoms (argon). Metal atoms ejected from the target by the ionized gas cross the plasma to deposit onto any surface within the coating unit including the specimen. A low vacuum environment, ~ 0.1 to 0.05 mbar is used with one of the modern low voltage sputter coaters that enables metal to be deposited at upto 1nm/s. Sputtered metals are deposited in the form of islands and not as continuous coating.

2.3 Photocatalytic Activity

Photocatalytic property of selective compounds was studied by way of dye degradation of a model dye, methylene blue (MB). MB is a basic dye which is extensively used in textile

industry. MB exists in crystalline form and when dissolved in water it appears dark blue (oxidised state) in colour and gives intense absorption at 664 nm (λ_{max}). Molecular formula of MB is $C_{16}H_{18}ClN_3S$ and the chemical structure is shown in Figure 2.1.
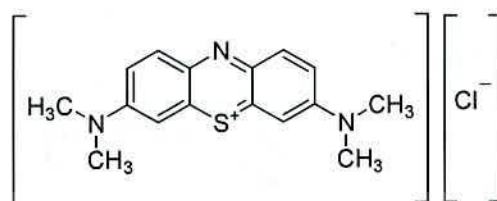
Methylene Blue

Figure 2.1: Structure of Methylene Blue

The activity of the compounds towards MB degradation under visible light was investigated. To evaluate the potential of the photocatalysts, the effect of catalyst concentration and irradiation time on the dye degradation were investigated. After the optimization of irradiation time, the dependence of catalyst concentration on dye degradation was investigated.

CHAPTER-III

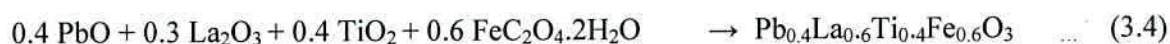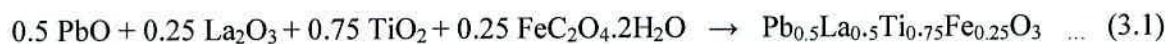# Synthesis and Characterization of Transition Metal-substituted Perovskite Titanates

3.1 Synthesis

We have investigated the synthesis of transition metal-substituted lead-lanthanum titanates of the general composition, $Pb_{1-x}La_xTi_{1-x/2}M_{x/2}O_3$ (M = Fe, Co, Mn) by solid state reaction method. In a typical solid state synthesis, stoichiometric quantities of PbO, La_2O_3, TiO_2 (Anatase) and $MC_2O_4.2H_2O$ (M = Fe, Co, Mn) were thoroughly mixed and reacted as described in the experimental section (Chapter-II). The standardized reaction conditions for the synthesis of respective compositions are presented in Table 3.1.

Table 3.1: Chemical compositions and reaction conditions for perovskite titanates, $Pb_{1-x}La_xTi_{1-x/2}M_{x/2}O_3$ (M = Fe, Co, Mn) and $Pb_{0.4}La_{0.6}Ti_{0.7}Fe_{0.3}O_3$.

Sl. No.	Compound	Reaction conditions
1	$Pb_{0.5}La_{0.5}Ti_{0.75}Fe_{0.25}O_3$	$750°C$ / 12hrs, $850°C$ / 12hrs + 24hrs, $900°C$ / 24hrs
2	$Pb_{0.5}La_{0.5}Ti_{0.75}Mn_{0.25}O_3$	$750°C$ / 12hrs, $850°C$ / 12hrs + 24hrs, $900°C$ / 24hrs
3	$Pb_{0.5}La_{0.5}Ti_{0.75}Co_{0.25}O_3$	$750°C$ / 12hrs, $850°C$ / 12hrs + 24hrs, $900°C$ / 24hrs
4	$Pb_{0.4}La_{0.6}Ti_{0.4}Fe_{0.6}O_3$	$750°C$ / 12hrs, $850°C$ / 12hrs + 24hrs
5	$Pb_{0.4}La_{0.6}Ti_{0.7}Fe_{0.3}O_3$	$750°C$ /12hrs, $850°C$ /12hrs + 24hrs

The stoichiometries of the starting materials and the final composition that would form single phase compounds are represented by the following equations (3.1) – (3.5).

$$0.5\ PbO + 0.25\ La_2O_3 + 0.75\ TiO_2 + 0.25\ FeC_2O_4.2H_2O \rightarrow Pb_{0.5}La_{0.5}Ti_{0.75}Fe_{0.25}O_3 \quad ... \quad (3.1)$$

$$0.5\ PbO + 0.25\ La_2O_3 + 0.75\ TiO_2 + 0.25\ MnC_2O_4.2H_2O \rightarrow Pb_{0.5}La_{0.5}Ti_{0.75}Mn_{0.25}O_3 \quad ... \quad (3.2)$$

$$0.5\ PbO + 0.25\ La_2O_3 + 0.75\ TiO_2 + 0.25\ CoC_2O_4.2H_2O \rightarrow Pb_{0.5}La_{0.5}Ti_{0.75}Co_{0.25}O_3 \quad ... \quad (3.3)$$

$$0.4\ PbO + 0.3\ La_2O_3 + 0.4\ TiO_2 + 0.6\ FeC_2O_4.2H_2O \rightarrow Pb_{0.4}La_{0.6}Ti_{0.4}Fe_{0.6}O_3 \quad ... \quad (3.4)$$

$$0.4\ PbO + 0.3\ La_2O_3 + 0.7\ TiO_2 + 0.3\ FeC_2O_4.2H_2O \rightarrow Pb_{0.4}La_{0.6}Ti_{0.7}Fe_{0.3}O_3 \quad ... \quad (3.5)$$

3.2 Powder X-Ray Diffraction (PXD)

The progress of the solid state reaction and single phase formation were monitored by recording the PXD patterns of the samples obtained at the end of every heating cycle. The PXD patterns for $Pb_{0.5}La_{0.5}Ti_{0.75}Fe_{0.25}O_3$ at various stages of the reaction are shown in Figure 3.1. An analysis of the PXD pattern with the JCPDS files reported in the literature indicated formation of perovskite type phase similar to cubic $LaTiO_3$ (JCPDS card # 75-0267). After heating at 900°C in the final cycle, well defined and sharp reflections were observed in the PXD pattern that did not change further from the previous heating cycles. The unit cell parameter of the newly synthesized $Pb_{0.5}La_{0.5}Ti_{0.75}Fe_{0.25}O_3$ is determined by least-squares refinement of the observed reflections using the PROSZKI program [1]. Table 3.2 gives the indexing of the observed lines and the least-squared refined lattice parameter for $Pb_{0.5}La_{0.5}Ti_{0.75}Fe_{0.25}O_3$.

15

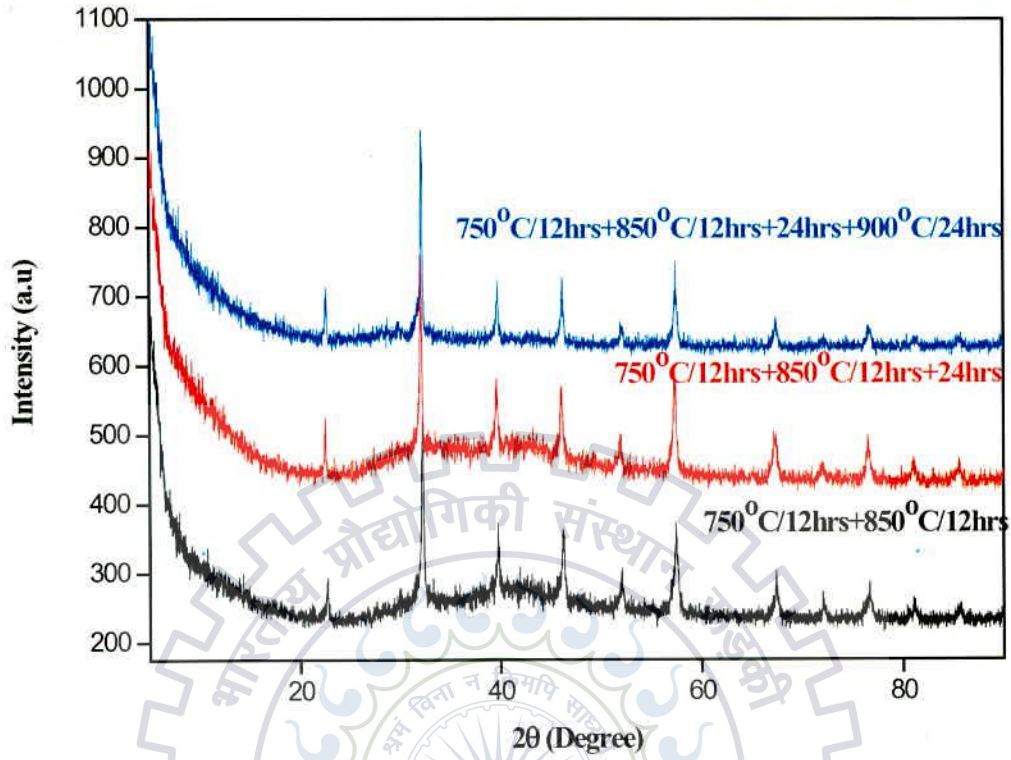**Figure 3.1:** PXD patterns of $Pb_{0.5}La_{0.5}Ti_{0.75}Fe_{0.25}O_3$ at different temperatures.

Table 3.2: PXD data for $Pb_{0.5}La_{0.5}Ti_{0.75}Fe_{0.25}O_3$.

h	k	l	d_{obs} (Å)	d_{calc} (Å)
1	0	0	3.9438	3.9354
1	1	0	2.7850	2.7827
1	1	1	2.2733	2.2721
2	0	0	1.9680	1.9677
2	1	0	1.7617	1.7599
2	1	1	1.6073	1.6066
2	2	0	1.3913	1.3913
3	0	0	1.3119	1.3118
3	1	0	1.2442	1.2444
3	1	1	1.1860	1.1865
2	2	2	1.1358	1.1360

Refined cell parameter, a = 3.9354 (5) Å.

After the successful synthesis of $Pb_{0.5}La_{0.5}Ti_{0.75}Fe_{0.25}O_3$, we have attempted to synthesize analogous titanates of similar composition with other transition metals, such as, Mn and Co. Figure 3.2 and 3.3 shows the PXD patterns for $Pb_{0.5}La_{0.5}Ti_{0.75}Mn_{0.25}O_3$ and $Pb_{0.5}La_{0.5}Ti_{0.75}Co_{0.25}O_3$, respectively, at various stages of the reaction. In case of the Mn- and Co-substituted perovskites, a comparison of the PXD patterns with the standard JCPDS files also showed formation of similar perovskite type phases to that that of Fe compound. The heatings were stopped at temperatures (Table 3.1) where no further changes were observed in the PXD patterns. The indexing of the PXD patterns are carried out with the PROSZKI [1] program. The indexed PXD data for $Pb_{0.5}La_{0.5}Ti_{0.75}Mn_{0.25}O_3$ and $Pb_{0.5}La_{0.5}Ti_{0.75}Co_{0.25}O_3$ are presented in Tables 3.3 and 3.4, respectively.
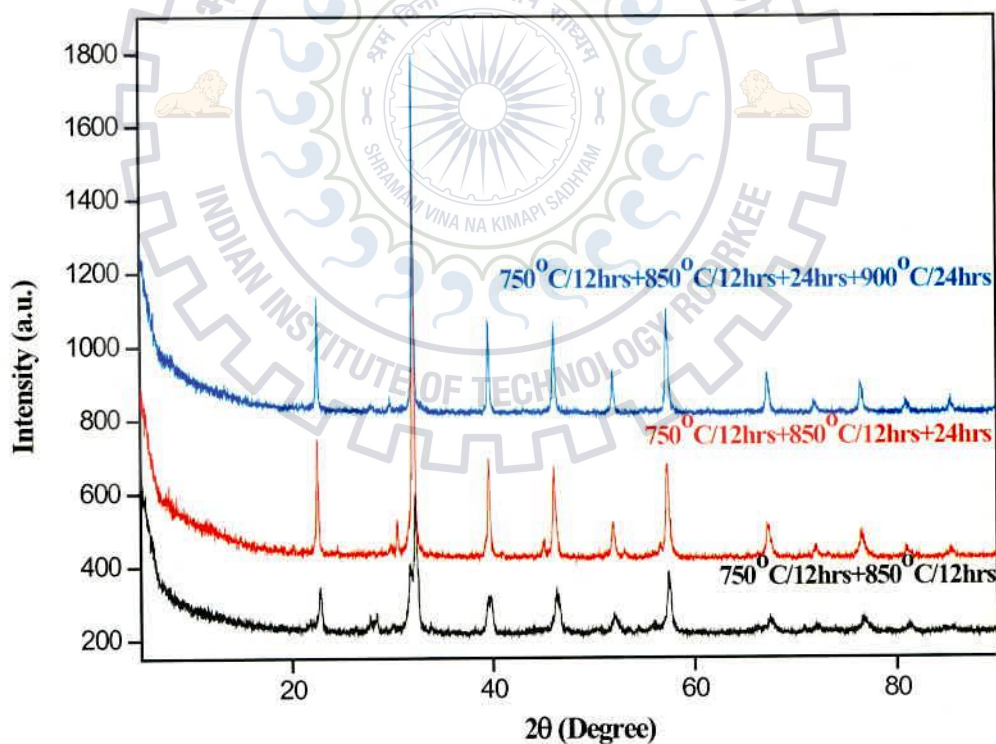

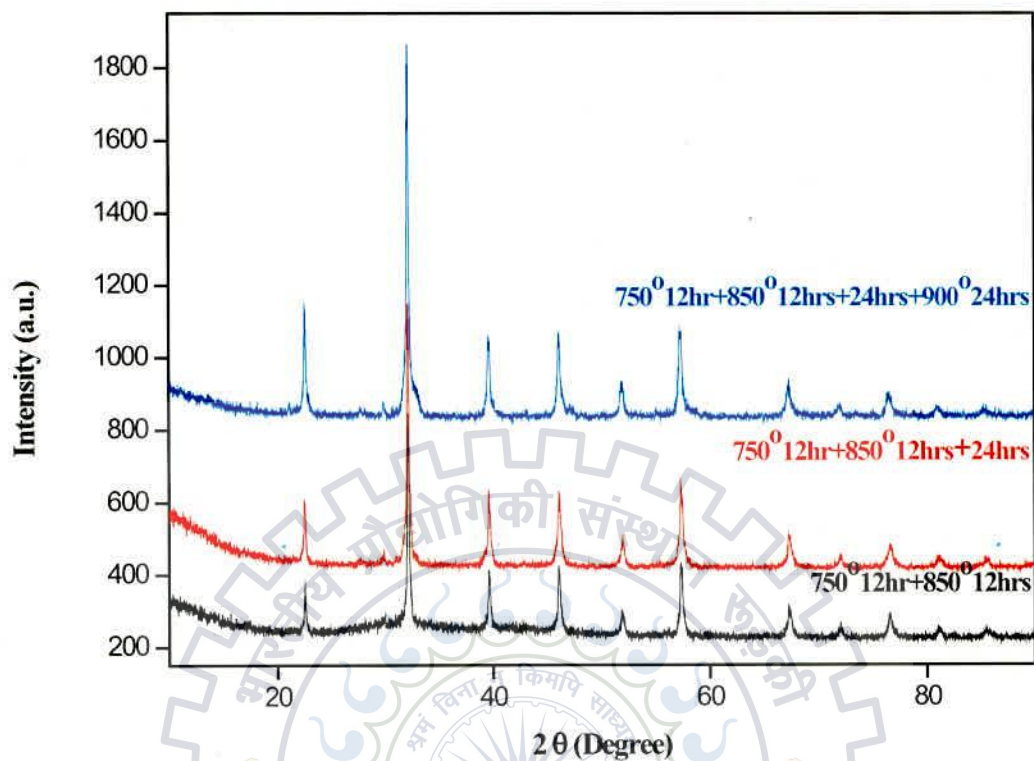Figure 3.2: PXD patterns of $Pb_{0.5}La_{0.5}Ti_{0.75}Mn_{0.25}O_3$ at different temperatures.

Figure 3.3: PXD patterns of $Pb_{0.5}La_{0.5}Ti_{0.75}Co_{0.25}O_3$ at different temperatures.

Table 3.3: PXD data for $Pb_{0.5}La_{0.5}Ti_{0.75}Mn_{0.25}O_3$.

h	*k*	*l*	d_{obs} (Å)	d_{calc} (Å)
1	0	0	3.9351	3.9359
1	1	0	2.7822	2.7831
1	1	1	2.2730	2.2724
2	0	0	1.9673	1.9679
2	1	0	1.7604	1.7602
2	1	1	1.6065	1.6068
2	2	0	1.3919	1.3915
3	0	0	1.3118	1.3119
3	1	0	1.2446	1.2446
3	1	1	1.1868	1.1867
2	2	2	1.1362	1.1362

Refined cell parameter, $a = 3.9359$ (2) Å.

18

Table 3.4: PXD data for $Pb_{0.5}La_{0.5}Ti_{0.75}Co_{0.25}O_3$.

h	k	l	d_{obs} (Å)	d_{calc} (Å)
1	0	0	3.9404	3.9341
1	1	0	2.7834	2.7818
1	1	1	2.2732	2.2713
2	0	0	1.9673	1.9670
2	1	0	1.7582	1.7594
2	1	1	1.6073	1.6061
2	2	0	1.3903	1.3909
3	0	0	1.3115	1.3113
3	1	0	1.2438	1.2441
3	1	1	1.1862	1.1862
2	2	2	1.1356	1.1357

Refined cell parameter, $a = 3.9341$ (5) Å.

In the newly synthesized perovskite series of compounds, $Pb_{0.5}La_{0.5}Ti_{0.75}M_{0.25}O_3$ (M = Fe, Co, Mn), a comparison of the cell parameters indicate that as compared to Fe and Mn analogue, the Co compound is having a larger cell parameter. The elemental ratios of Pb, La and Ti being the same in all the three compounds, this is solely due to the transition metal. Moreover, for charge neutrality of the composition the transition metal would be in the 2+ state. In the perovskite oxide lattice, the transition metal is octahedrally coordinated by oxygen ligands and oxygen being a weak field ligand will give rise to high spin complexes. All the three transition metals (M^{2+} = Mn, Fe, Co) in the high spin configuration are not strong Jahn-Teller ions. Therefore, no significant Jahn-Teller distortion is expected and consequently all the compounds form in a cubic perovskite structure. Moreover, even if there is a weak Jahn-Teller distortion, given the amount of substituted transition metal (0.25) as compared to the other B-site metal (0.75), it may not be significant enough to lower the symmetry of the lattice.

Our attempts to synthesize the nominal perovskite compositions, $Pb_{0.75}La_{0.25}Ti_{0.75}M_{0.25}O_3$ (M = Mn, Fe, Co), was not successful. The exact reason is not known at present, why the phases could not be stabilized. If such a composition could have formed, the transition metal would have been stabilized in the 3+ oxidation state. Nonetheless, we have further envisaged compositions, such as, $Pb_{0.4}La_{0.6}Ti_{0.4}Fe_{0.6}O_3$ and $Pb_{0.4}La_{0.6}Ti_{0.7}Fe_{0.3}O_3$, where for the compositional neutrality, Fe would be in the 3+ and 2+ states, respectively. To our surprise, both the compositions were stabilized by stoichiometric solid state reactions of its constituents similar to those described earlier (Table 3.1).

Formation of single phase compositions, $Pb_{0.4}La_{0.6}Ti_{0.4}Fe_{0.6}O_3$ and $Pb_{0.4}La_{0.6}Ti_{0.7}Fe_{0.3}O_3$, were analyzed by PXD. Figures 3.4 & 3.5 shows the PXD patterns obtained at various reaction conditions.

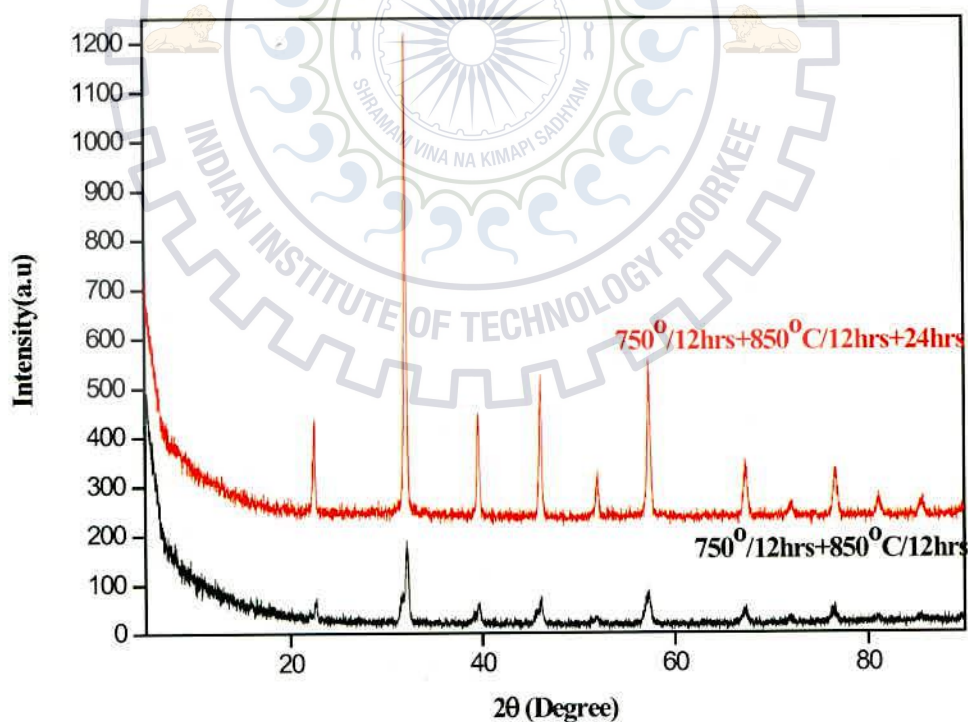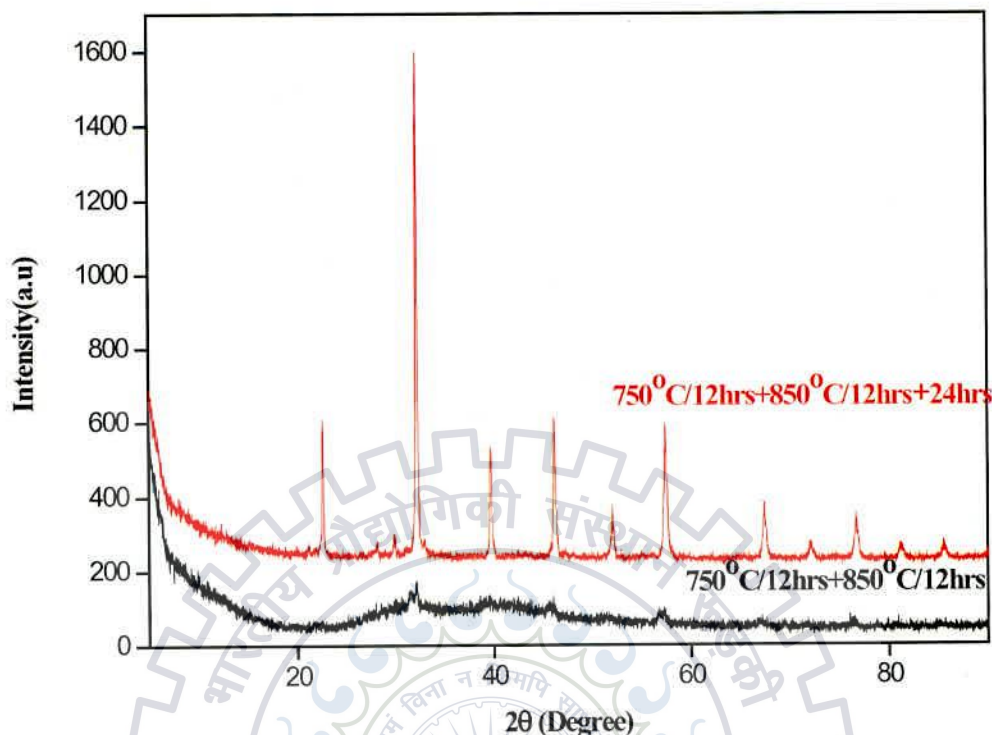**Figure 3.4: PXD patterns of $Pb_{0.4}La_{0.6}Ti_{0.4}Fe_{0.6}O_3$ at different temperatures.**

Figure 3.5: PXD patterns of $Pb_{0.4}La_{0.6}Ti_{0.7}Fe_{0.3}O_3$ at different temperatures.

Comparison of PXD patterns with standard JCPDS files again indicated cubic perovskite like phases. The lattice parameters for the compositions, $Pb_{0.4}La_{0.6}Ti_{0.4}Fe_{0.6}O_3$ and $Pb_{0.4}La_{0.6}Ti_{0.7}Fe_{0.3}O_3$, were least-square fitted by PROSZKOI program [1]. Tables 3.5 & 3.6 give the indexing data for these two compounds. In case of $Pb_{0.4}La_{0.6}Ti_{0.7}Fe_{0.3}O_3$, three un-indexed small intensity reflections observed at 28.09, 29.82 and 32.87° are attributed to some unidentified impurity. It is interesting to note that both the compounds have very similar lattice parameters despite having different composition and transition metal content. This can be explained by the fact that Fe is in 3+ state in $Pb_{0.4}La_{0.6}Ti_{0.4}Fe_{0.6}O_3$, while it is in 2+ state in $Pb_{0.4}La_{0.6}Ti_{0.7}Fe_{0.3}O_3$ to satisfy charge neutrality. Therefore, a contraction in lattice for $Pb_{0.4}La_{0.6}Ti_{0.7}Fe_{0.3}O_3$ due to larger amount of Ti^{4+} as compared to that of $Pb_{0.4}La_{0.6}Ti_{0.4}Fe_{0.6}O_3$,

21

is compensated by an expansion in lattice due to the presence of Fe^{2+} in the former, instead of Fe^{3+} in the later.

Table 3.5: PXD data for $Pb_{0.4}La_{0.6}Ti_{0.4}Fe_{0.6}O_3$.

h	k	l	d_{obs} (Å)	d_{calc} (Å)
1	0	0	3.9407	3.9301
1	1	0	2.7836	2.7790
1	1	1	2.2725	2.2690
2	0	0	1.9666	1.9650
2	1	0	1.7572	1.7576
2	1	1	1.6053	1.6044
2	2	0	1.3893	1.3895
3	0	0	1.3095	1.3100
3	1	0	1.2424	1.2428
3	1	1	1.1851	1.1849
2	2	2	1.1341	1.1345

Refined cell parameter, $a = 3.9301$ (7) Å.

Table 3.6: PXD data for $Pb_{0.4}La_{0.6}Ti_{0.7}Fe_{0.3}O_3$.

h	k	l	d_{obs} (Å)	d_{calc} (Å)
1	0	0	3.9284	3.9300
1	1	0	2.7787	2.7789
1	1	1	2.2701	2.2690
2	0	0	1.9657	1.9650
2	1	0	1.7570	1.7575
2	1	1	1.6049	1.6044
2	2	0	1.3889	1.3894
3	0	0	1.3098	1.3100
3	1	0	1.2423	1.2428
3	1	1	1.1852	1.1849
2	2	2	1.1348	1.1345

Refined cell parameter, $a = 3.9301$ (4) Å.

A simulation of the PXD data based on a cubic perovskite structure has been carried out for $Pb_{0.5}La_{0.5}Ti_{0.75}Fe_{0.25}O_3$ in *Pm-3m* space group with standard positional parameters, where only fractional occupancies are adjusted according to the composition (Table 3.7). Figure 3.6 shows the observed and simulated PXD patterns for $Pb_{0.5}La_{0.5}Ti_{0.75}Fe_{0.25}O_3$. There is an excellent agreement with the position and relative intensity of all the reflections confirming a cubic perovskite structure for $Pb_{0.5}La_{0.5}Ti_{0.75}Fe_{0.25}O_3$.

Table 3.7: Positional, occupancy and thermal parameters used for simulation.*

Atom	x	y	z	Occ.	$B\ (\text{Å}^2)$
Pb	0.5	0.5	0.5	0.5	0.2
La	0.5	0.5	0.5	0.5	0.2
Ti	0.0	0.0	0.0	0.75	0.4
Fe	0.0	0.0	0.0	0.25	0.4
O	0.5	0.0	0.0	1.0	1.0

* Unit cell parameter, a = 3.9354 Å.
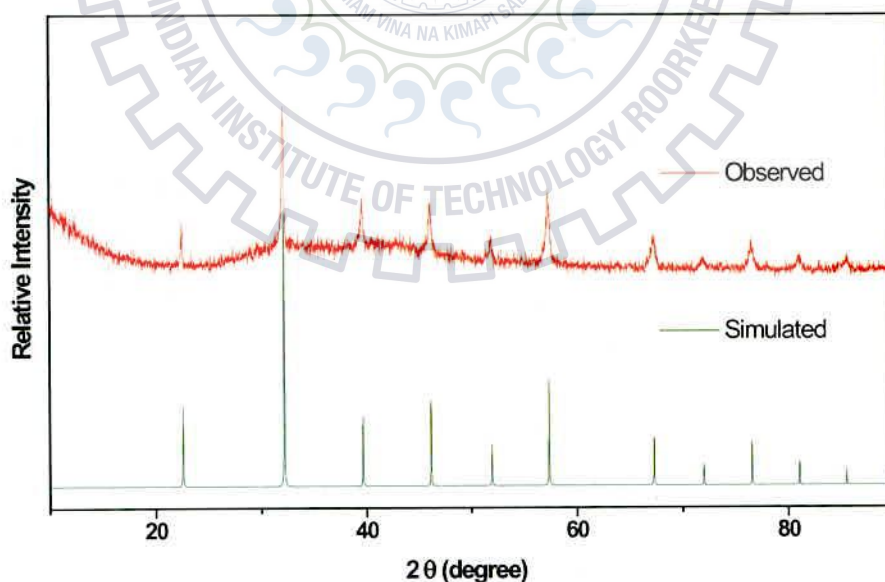
Figure 3.6: Observed and simulated PXD patterns of $Pb_{0.5}La_{0.5}Ti_{0.75}Fe_{0.25}O_3$.

3.3 FE-SEM and EDX Analysis

The morphology of crystallite and chemical composition of the synthesized compounds were investigated by FE-SEM and EDX analysis, respectively. Figure 3.7 shows SEM images of $Pb_{0.5}La_{0.5}Ti_{0.75}Fe_{0.25}O_3$ at different magnifications (a) 5000×, (b) 10000×, (c) & (d) 20000×. The images in (a) and (b) shows homogeneous morphologies throughout the entire region of imaging. However, a closer look at a higher magnification (20000×) showed some distinctly different morphology. In (c) uniformly agglomerated particles are seen while in (d) plate like crystallites are stuck in bigger agglomerate. We have analysed the elemental ratios at large selected areas as well as at different crystallites on spot basis analysis. Figure 3.8 shows the SEM images (a & b), corresponding EDX spectra (c & d) and elemental percentages (e & f) taken in the specified region or spot for as synthesized $Pb_{0.5}La_{0.5}Ti_{0.75}Fe_{0.25}O_3$. The EDX spectra taken at several crystallites of the imaged area shown in (a) shows very good compositional uniformity with the nominal elemental composition. However, the EDX spectra taken on the imaged area (b), did show some inhomogeneity and compositional fluctuation as given in panel (f). The data shows depletion in Pb and Fe and enhancement in La and Ti content. This could be due to some clustering/accumulation of specific elements in certain region due to inhomogeneous mixing of the starting compounds. Moreover, this type of region was not observed at large numbers, but could be located only in few places. In the PXD data, we did not find any supplementary information in terms of separate phase formation with the appearance of additional reflections. This could possibly indicate the presence of a small amount of additional impurity phase below the detection limit of PXD. The other probability, which could not be ruled out is the similarity of the unit cell parameters of the unknown impurity phase (with the same cubic perovskite

24

structure) with the main phase of the nominal composition. In such a scenario, the peaks will overlap and be subsided by the major phase.
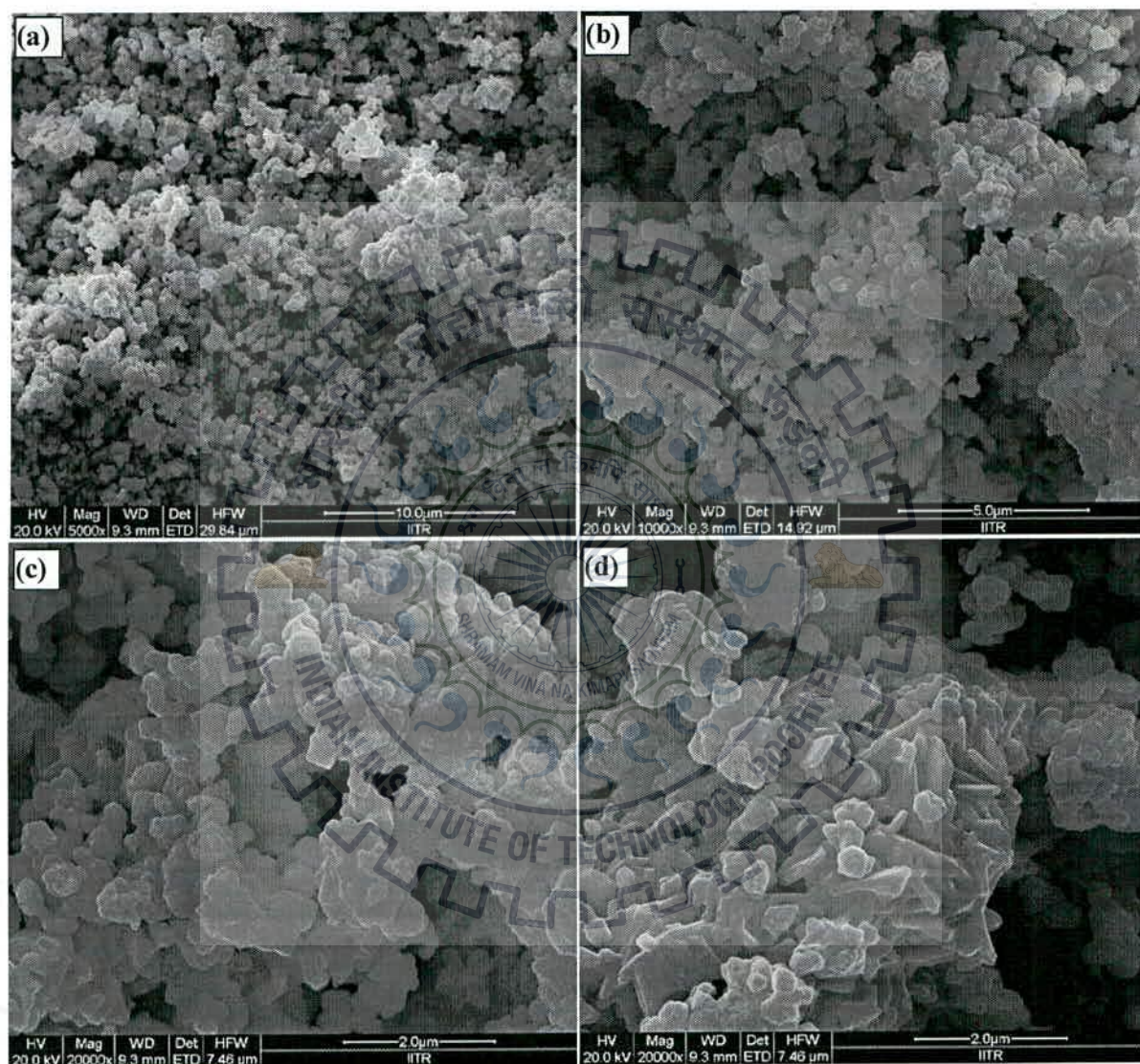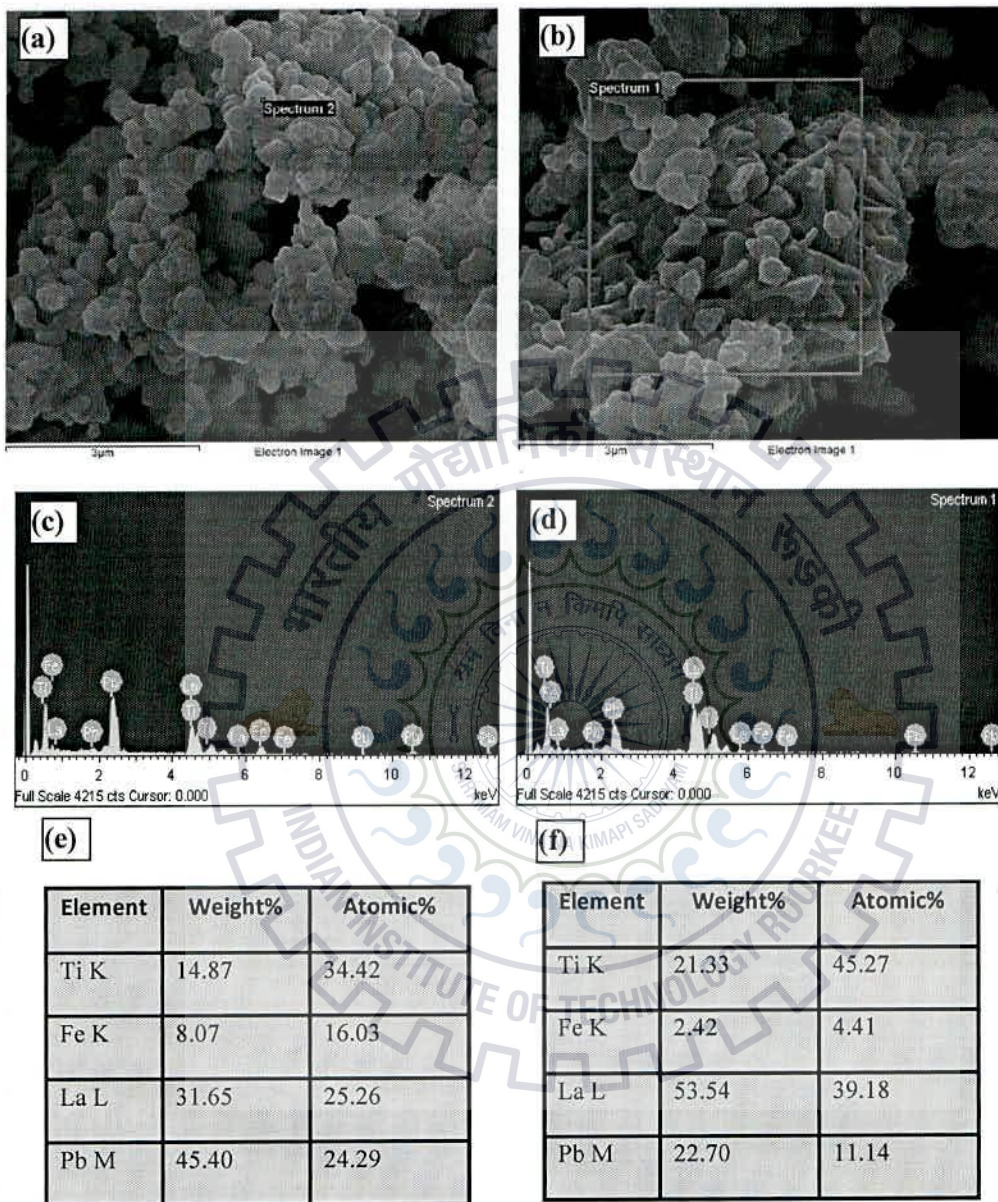

Figure 3.7: SEM images of the as synthesized $Pb_{0.5}La_{0.5}Ti_{0.75}Fe_{0.25}O_3$ sample at different magnifications, (a) 5000×, (b) 10000×, (c) & (d) 20000×.

Element	Weight%	Atomic%
Ti K	14.87	34.42
Fe K	8.07	16.03
La L	31.65	25.26
Pb M	45.40	24.29

Element	Weight%	Atomic%
Ti K	21.33	45.27
Fe K	2.42	4.41
La L	53.54	39.18
Pb M	22.70	11.14

Figure 3.8: SEM images (a & b), corresponding EDX spectra (c & d) and elemental percentages (e & f) taken in the specified region or spot for as synthesized $Pb_{0.5}La_{0.5}Ti_{0.75}Fe_{0.25}O_3$.

SEM images of the as synthesized $Pb_{0.5}La_{0.5}Ti_{0.75}Mn_{0.25}O_3$ (a & b) and $Pb_{0.5}La_{0.5}Ti_{0.75}Co_{0.25}O_3$ (c & d) at different magnifications, (a) & (c) 10000×; (b) & (d) 20000×, are shown in Figure 3.9. The images in (a) and (b) show homogeneous morphologies throughout the entire region of imaging for $Pb_{0.5}La_{0.5}Ti_{0.75}Mn_{0.25}O_3$. Similarly, images in (c) and (d) show homogeneous morphologies throughout the entire region of imaging for $Pb_{0.5}La_{0.5}Ti_{0.75}Co_{0.25}O_3$. The SEM images (a & d), corresponding EDX spectra (b & e) and elemental percentages (c & f) for $Pb_{0.5}La_{0.5}Ti_{0.75}Mn_{0.25}O_3$ and $Pb_{0.5}La_{0.5}Ti_{0.75}Co_{0.25}O_3$, respectively, are shown in Figure 3.10. The EDX spectra taken at several crystallites of the imaged area shown in (a) and (d) for $Pb_{0.5}La_{0.5}Ti_{0.75}Mn_{0.25}O_3$ and $Pb_{0.5}La_{0.5}Ti_{0.75}Co_{0.25}O_3$, respectively, show very good compositional uniformity with the nominal elemental composition given in panel (c) and (f).

SEM images of the as synthesized $Pb_{0.4}La_{0.6}Ti_{0.4}Fe_{0.6}O_3$ (a & b) and $Pb_{0.4}La_{0.6}Ti_{0.7}Fe_{0.3}O_3$ (c & d) at different magnifications, (a) & (c) 10000×; (b) & (d) 20000×, are shown in Figure 3.11. Both the compositions show morphological homogeneity in the imaged region. Figure 3.12 shows the SEM images (a & d) along with the corresponding EDX spectra (b & e) and elemental percentages (c & f) for $Pb_{0.4}La_{0.6}Ti_{0.4}Fe_{0.6}O_3$ and $Pb_{0.4}La_{0.6}Ti_{0.7}Fe_{0.3}O_3$, respectively. For both the compositions, the elemental ratios obtained (panel c & f) from EDX spectra are in good agreement as expected for the nominal composition. Although, from PXD analysis of $Pb_{0.4}La_{0.6}Ti_{0.7}Fe_{0.3}O_3$, we have identified three small intensity reflections arising out of some unidentified impurity at 28.09, 29.82 and 32.87°, but in SEM-EDX analysis we could not identify any such region of non-perovskite composition.
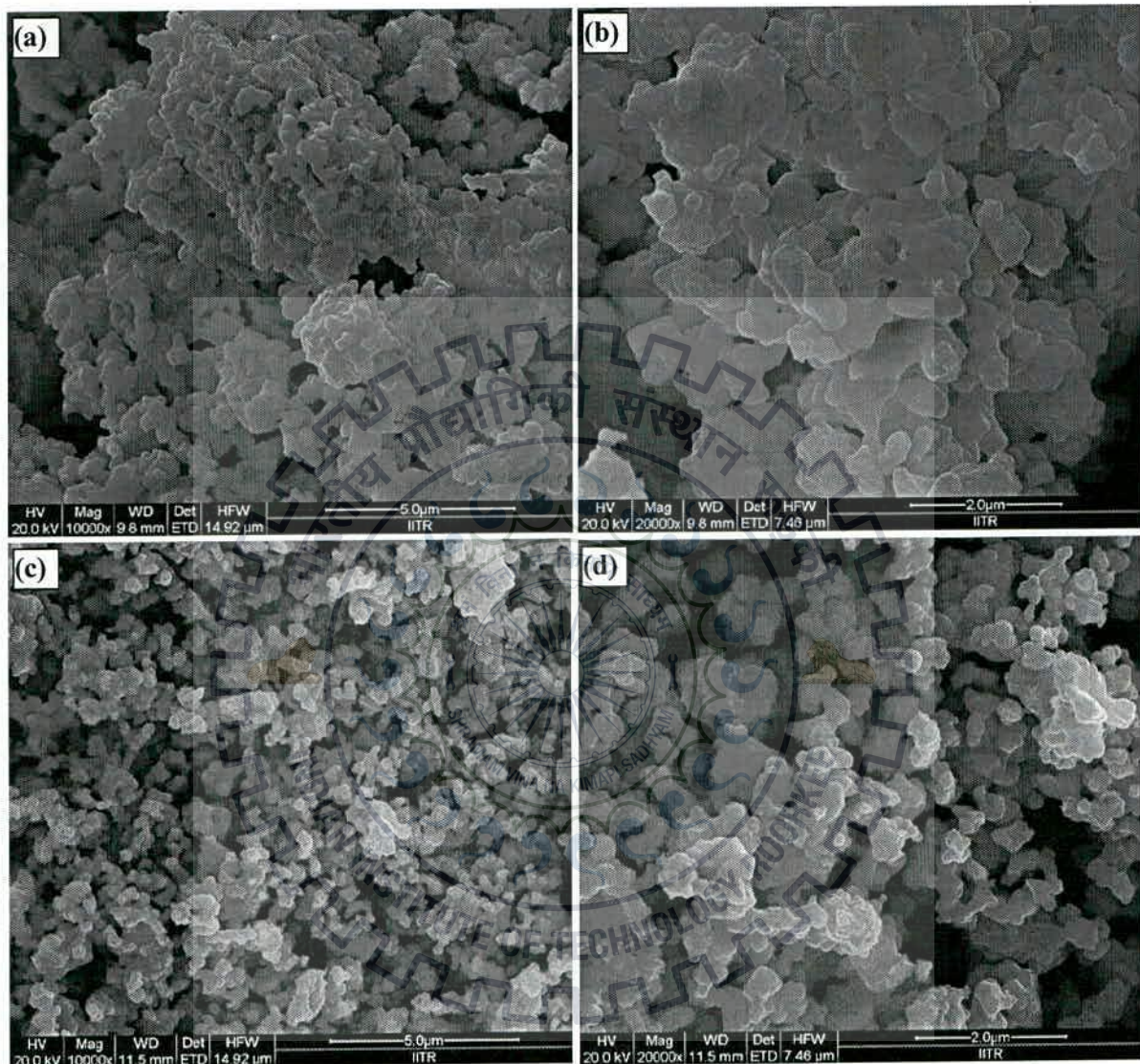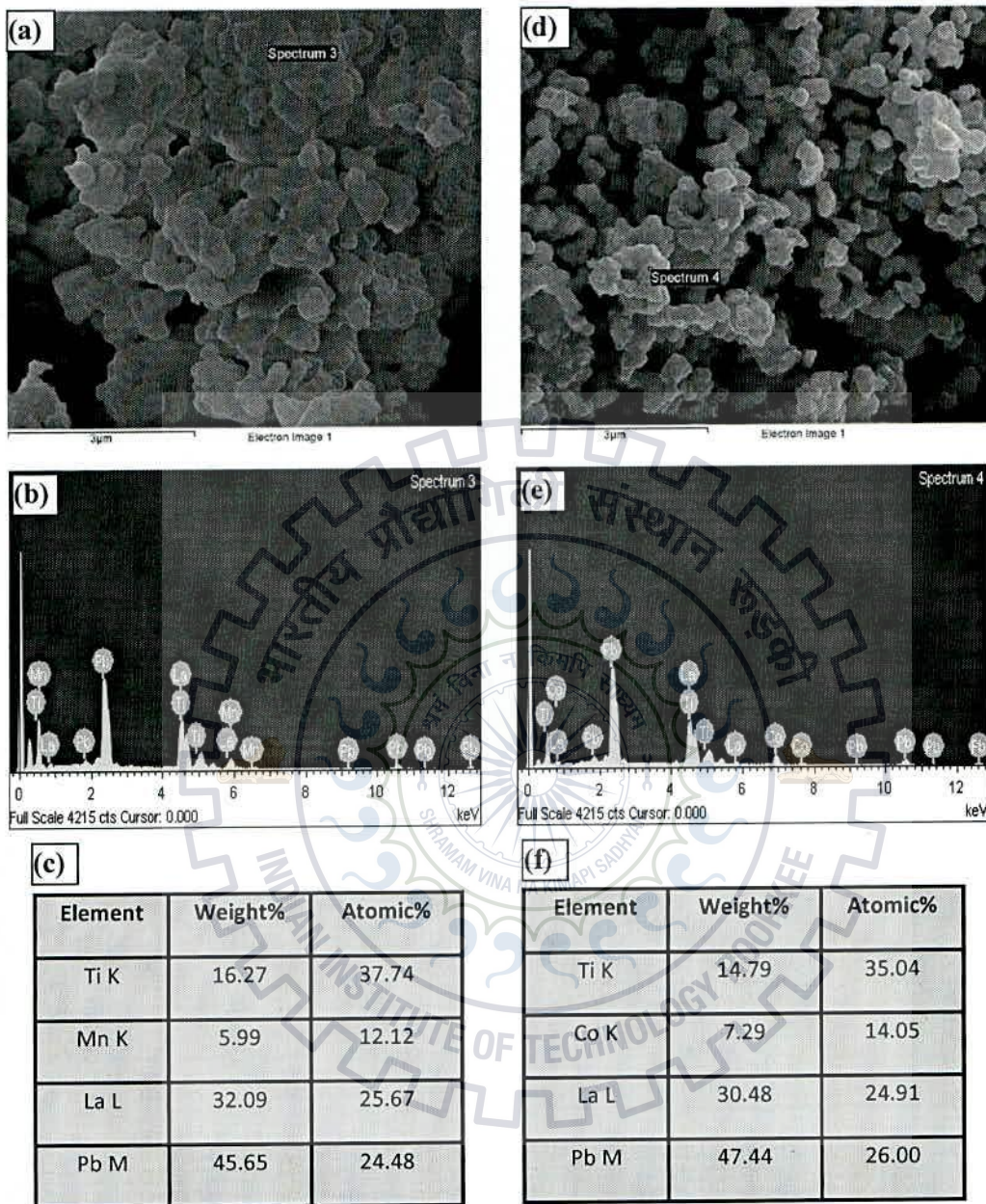
Figure 3.9: SEM images of as synthesized $Pb_{0.5}La_{0.5}Ti_{0.75}Mn_{0.25}O_3$ (a & b) and $Pb_{0.5}La_{0.5}Ti_{0.75}Co_{0.25}O_3$ (c & d) at different magnifications; (a) & (c) 10000×; (b) & (d) 20000×.

Figure 3.10: SEM images (a & d), corresponding EDX spectra (b & e) and elemental percentages (c & f) for $Pb_{0.5}La_{0.5}Ti_{0.75}Mn_{0.25}O_3$ and $Pb_{0.5}La_{0.5}Ti_{0.75}Co_{0.25}O_3$, respectively.
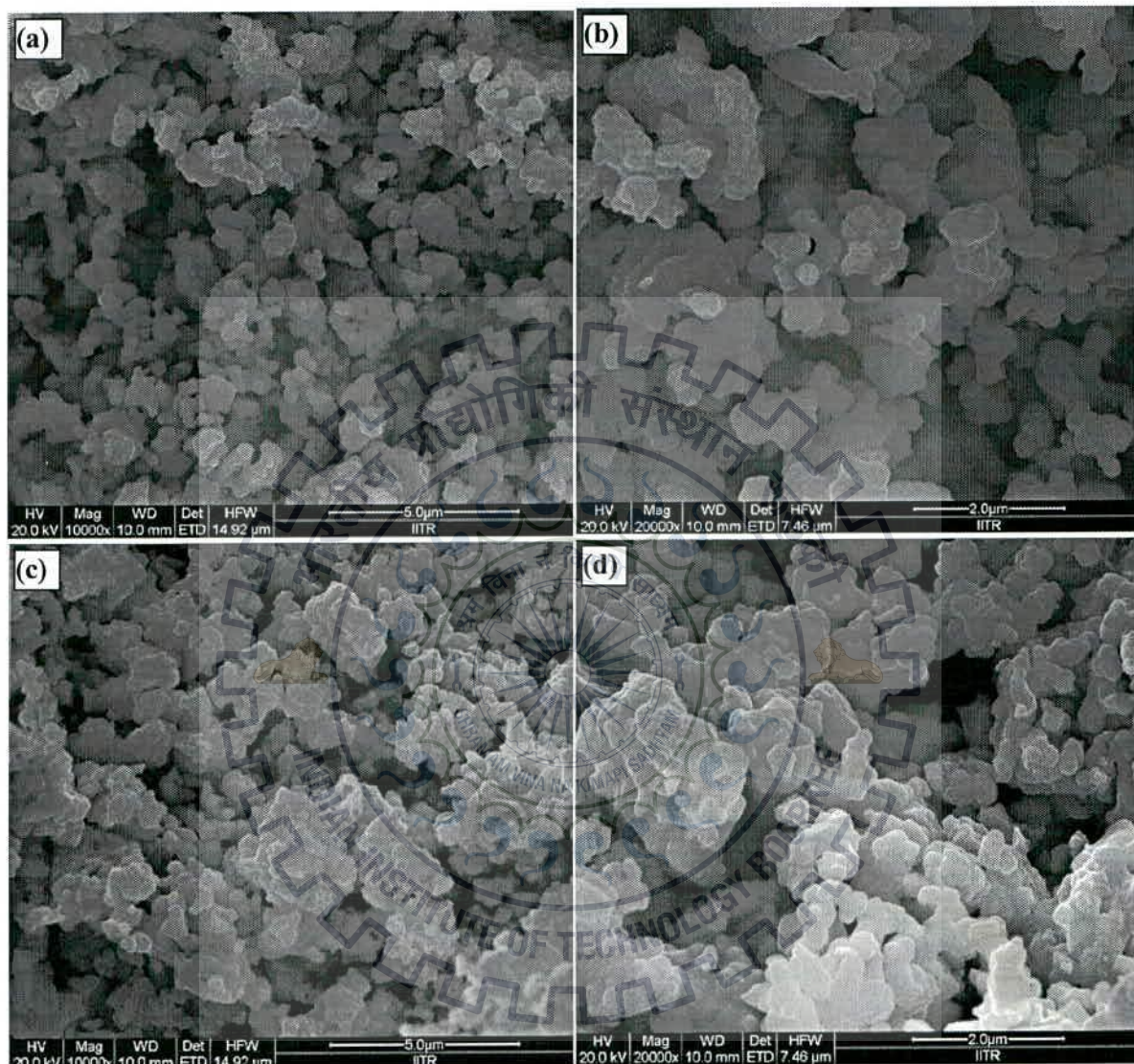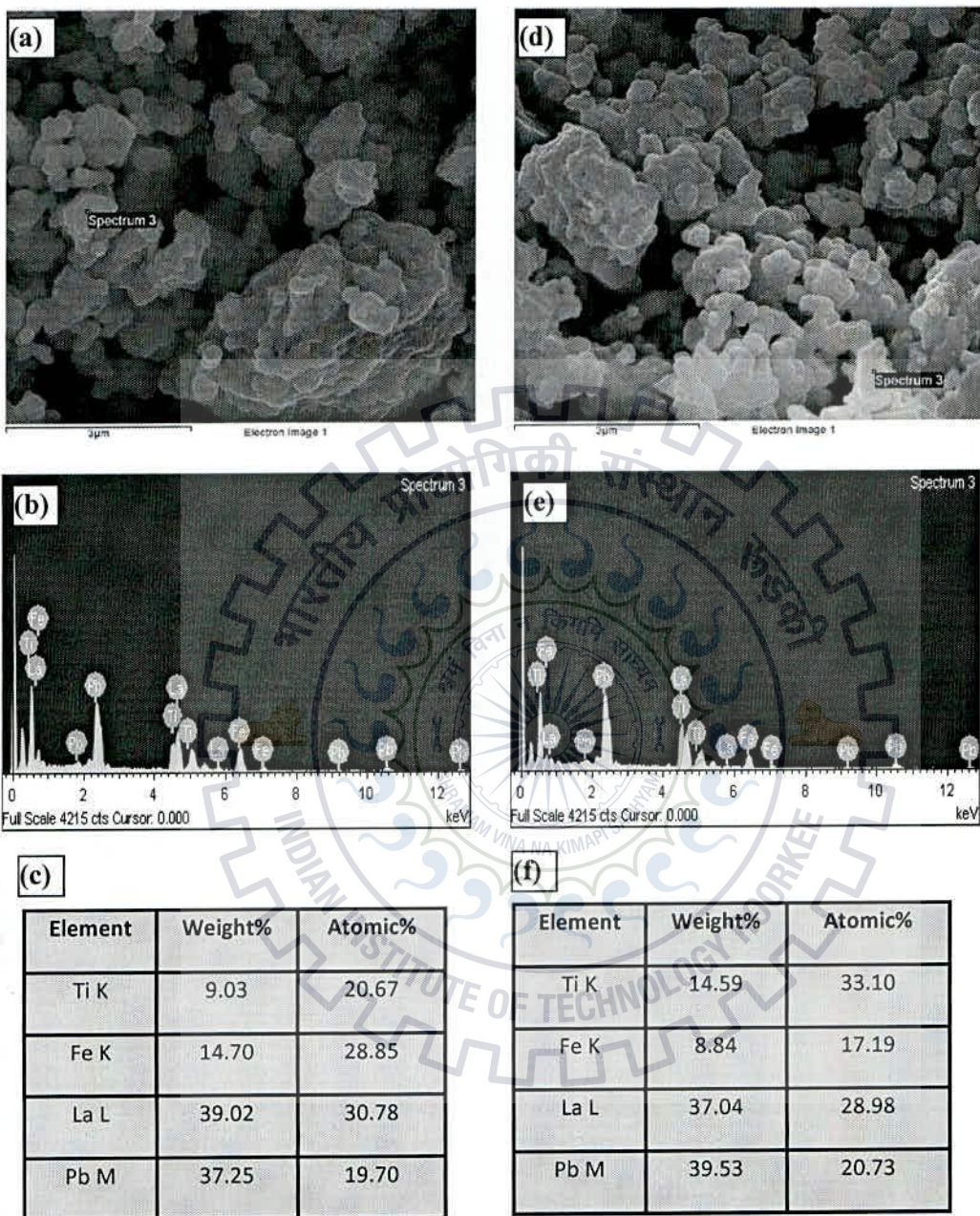
Figure 3.11: SEM images of as synthesized $Pb_{0.4}La_{0.6}Ti_{0.4}Fe_{0.6}O_3$ (a & b) and $Pb_{0.4}La_{0.6}Ti_{0.7}Fe_{0.3}O_3$ (c & d) at different magnifications; (a) & (c) 10000×; (b) & (d) 20000×.

(c)

Element	Weight%	Atomic%
Ti K	9.03	20.67
Fe K	14.70	28.85
La L	39.02	30.78
Pb M	37.25	19.70

(f)

Element	Weight%	Atomic%
Ti K	14.59	33.10
Fe K	8.84	17.19
La L	37.04	28.98
Pb M	39.53	20.73

Figure 3.12: SEM images (a & d), corresponding EDX spectra (b & e) and elemental percentages (c & f) for $Pb_{0.4}La_{0.6}Ti_{0.4}Fe_{0.6}O_3$ and $Pb_{0.4}La_{0.6}Ti_{0.7}Fe_{0.3}O_3$, respectively.

3.4 UV-Visible Diffuse Reflectance Spectroscopy (UV-Vis DRS)

UV-Vis DRS spectra for $Pb_{0.5}La_{0.5}Ti_{0.75}Fe_{0.25}O_3$ are shown in Figure 3.13. The UV-vis DRS shows that the absorption edges for this compound is greater than 400 nm. The compound absorbs in the visible region. The band gap calculated by using equation (2.2) given in the experimental section (Chapter-II) is found to be 2.11 eV.
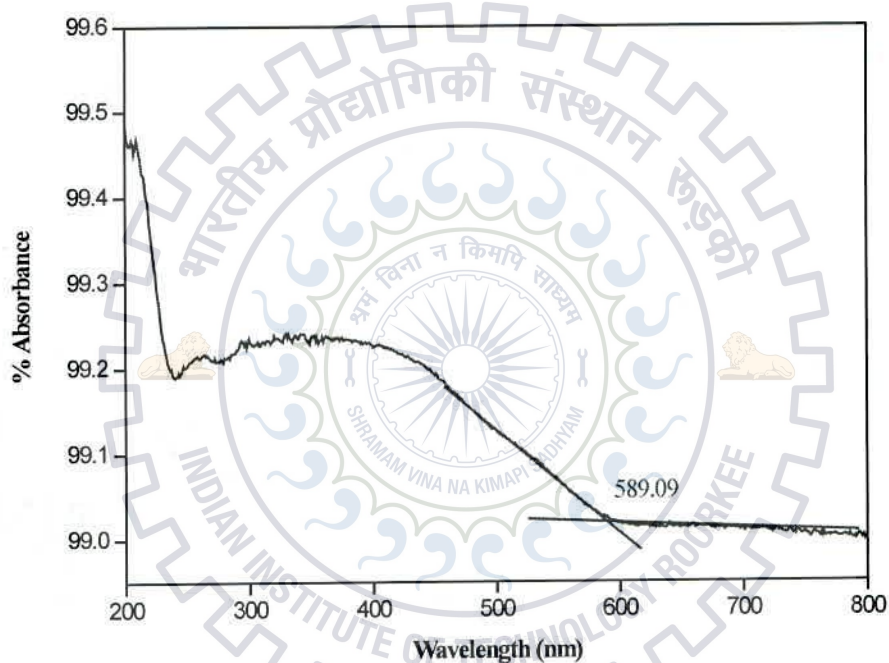

Figure 3.13: UV-Visible diffuse reflectance spectra of $Pb_{0.5}La_{0.5}Ti_{0.75}Fe_{0.25}$.

The UV-Vis DRS spectra for $Pb_{0.5}La_{0.5}Ti_{0.75}Mn_{0.25}O_3$, $Pb_{0.5}La_{0.5}Ti_{0.75}Co_{0.25}O_3$, $Pb_{0.4}La_{0.6}Ti_{0.4}Fe_{0.7}O_3$ and $Pb_{0.4}La_{0.6}Ti_{0.7}Fe_{0.3}O_3$ are given in Figures 3.14 - 3.17, respectively.

32
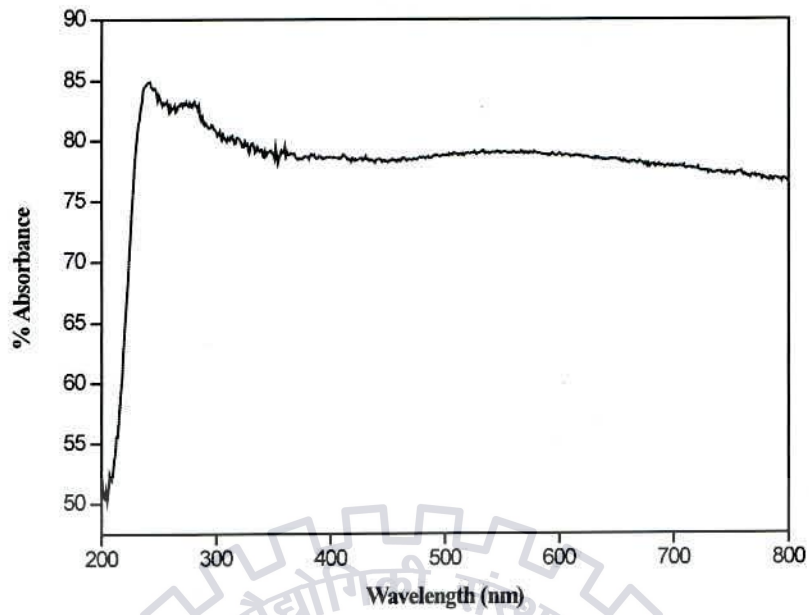
Figure 3.14: UV-Vis DRS spectra of $Pb_{0.5}La_{0.5}Ti_{0.75}Mn_{0.25}O_3$.
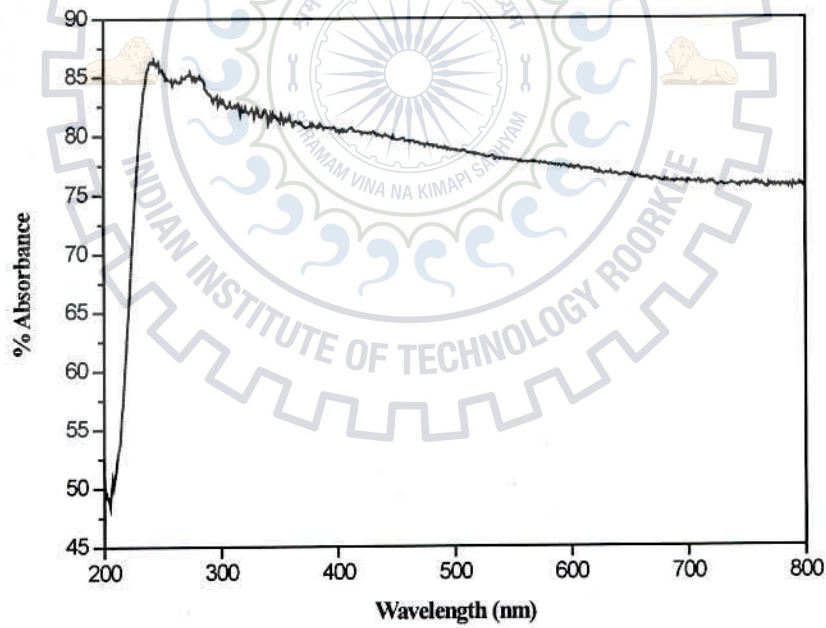
Figure 3.15: UV-Vis DRS spectra of $Pb_{0.5}La_{0.5}Ti_{0.75}Co_{0.25}O_3$.
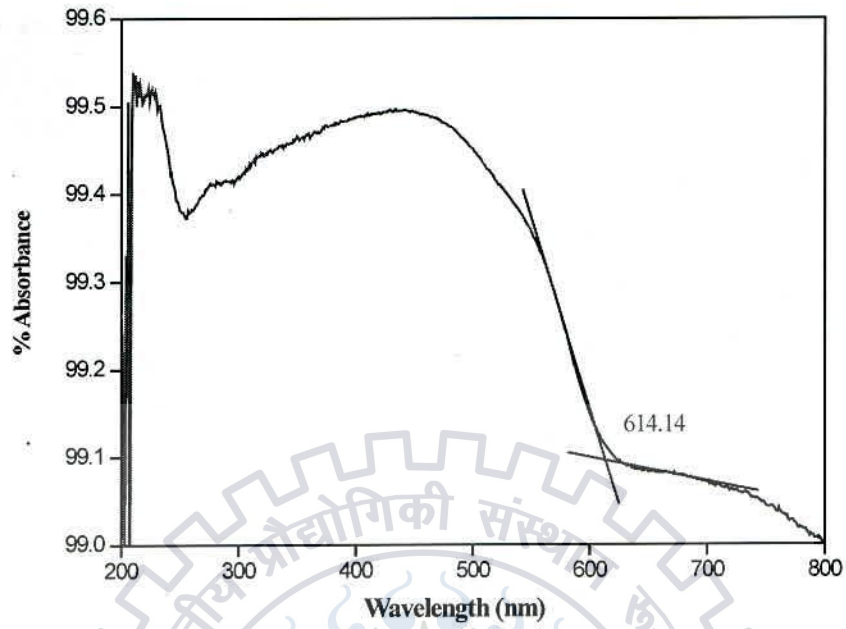
Figure 3.16: UV-Vis DRS spectra of Pb$_{0.4}$La$_{0.6}$Ti$_{0.4}$Fe$_{0.7}$O$_3$.
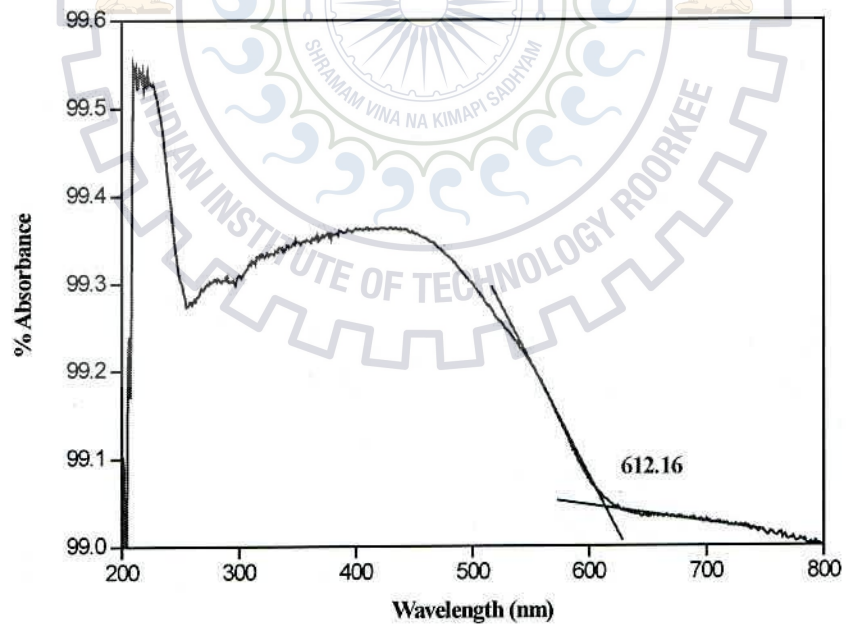
Figure 3.17: UV-Vis DRS spectra of Pb$_{0.4}$La$_{0.6}$Ti$_{0.7}$Fe$_{0.3}$O$_3$.

The UV-Vis DRS for $Pb_{0.5}La_{0.5}Ti_{0.75}Mn_{0.25}O_3$ and $Pb_{0.5}La_{0.5}Ti_{0.75}Co_{0.25}O_3$ shows continuous absorption starting from the UV region extended till 800 nm and beyond, probably to the near infra red region. This could be due to the surface/impurity states of wide range of energies covering the entire visible region of the spectrum. Therefore, band gap for these two compounds could not be calculated. The band gap energies for $Pb_{0.4}La_{0.6}Ti_{0.4}Fe_{0.7}O_3$ and $Pb_{0.4}La_{0.6}Ti_{0.7}Fe_{0.3}O_3$ calculated from the UV-Vis DRS are 2.02 and 2.03 eV, respectively. We find that all the Fe-containing compounds have band gaps in the visible region and therefore, study of their photocatalytic activity could be interesting (see Chapter-V).

CHAPTER-IV

Synthesis and Characterization of Transition Metal-substituted Layered Perovskite Niobates

4.1 Synthesis

We have envisaged the synthesis of $KCa_{2-x}La_xNb_{3-x/2}M_{x/2}O_{10}$ (M = Fe, Mn, Co) by solid state reaction method as described in the experimental section (Chapter-II). For the synthesis of $KCa_{2-x}La_xNb_{3-x/2}M_{x/2}O_{10}$ (M = Fe, Mn, Co and $x = 0.40$), stoichiometric quantities of $KNbO_3$, $CaCO_3$, La_2O_3, Nb_2O_5, and oxalates of transition metals were ground thoroughly in an agate mortar for about 45 minutes to one hour. $KNbO_3$ was prepared by reacting 2.764 g of K_2CO_3 with 5.314 g of Nb_2O_5 at 800 $^\circ$C for 6 hrs. A slight excess of K_2CO_3 was used in this reaction to compensate the loss of K_2CO_3 due to volatilization at higher temperatures. Since K_2CO_3 is very hygroscopic, to minimize the exposure of moisture to bare K_2CO_3, first Nb_2O_5 was taken in a mortar and then K_2CO_3 was added and mixed immediately. The as synthesized $KNbO_3$ was characterized by PXD before use. The PXD pattern of $KNbO_3$ is shown in Appendix (Figure A1).

Table 4.1 summarizes the compounds and standardized reaction conditions for $KCa_{2-x}La_xNb_{3-x/2}M_{x/2}O_{10}$ (M = Fe, Mn, Co). The stoichiometries of the starting materials and

36

Table: 4.1: Chemical compositions and reaction conditions for $KCa_{2-x}La_xNb_{3-x/2}M_{x/2}O_{10}$ (M = Fe, Mn, Co).

Sl. No.	Compound	Reaction Condition
1	$KCa_{1.6}La_{0.4}Nb_{2.8}Fe_{0.2}O_{10}$	750°C/12hrs,850°C/24hrs,1050°C/24hrs,1100°C/24hrs
2	$KCa_{1.6}La_{0.4}Nb_{2.8}Mn_{0.2}O_{10}$	750°C/12hrs,850° C/24hrs,1050° C/24hrs,1100°C/24hrs
3	$KCa_{1.6}La_{0.4}Nb_{2.8}Co_{0.2}O_{10}$	750°C/12hrs,850° C/24hrs,1050°C/24hrs,1100°C/24hrs

the final composition that would form single phase compounds are represented by the following equations (4.1) – (4.3).

$$KNbO_3+1.6CaCO_3+0.2La_2O_3+0.9Nb_2O_5+0.2FeC_2O_4.2H_2O \rightarrow KCa_{1.6}La_{0.4}Nb_{2.8}Fe_{0.2}O_{10} \quad -- \quad (4.1)$$

$$KNbO_3+1.6CaCO_3+0.2La_2O_3+0.9Nb_2O_5+0.2MnC_2O_4.2H_2O \rightarrow KCa_{1.6}La_{0.4}Nb_{2.8}Mn_{0.2}O_{10} \quad -- (4.2)$$

$$KNbO_3+1.6CaCO_3+0.2La_2O_3+0.9Nb_2O_5+0.2CoC_2O_4.2H_2O \rightarrow KCa_{1.6}La_{0.4}Nb_{2.8}Co_{0.2}O_{10} \quad -- (4.3)$$

4.2 Powder X-Ray Diffraction (PXD)

The PXD patterns of prepared compounds were compared with the standard JCPDS files available in the diffraction database. Figure 4.1 shows the XRD pattern of Fe-substituted compound. A comparison for the PXD pattern with the standard JCPDS files indicated formation of DJ type layered perovskite phase similar to $KCa_2Nb_3O_{10}$ (JCPDS card # 35-1294). The indexing of the PXD data for the $KCa_{1.6}La_{0.4}Nb_{2.8}Fe_{0.2}O_{10}$ is given in Table 4.2. The PXD patterns of Mn and Co substituted compounds at various stages of the reaction are shown in Figures 4.2 and 4.3.
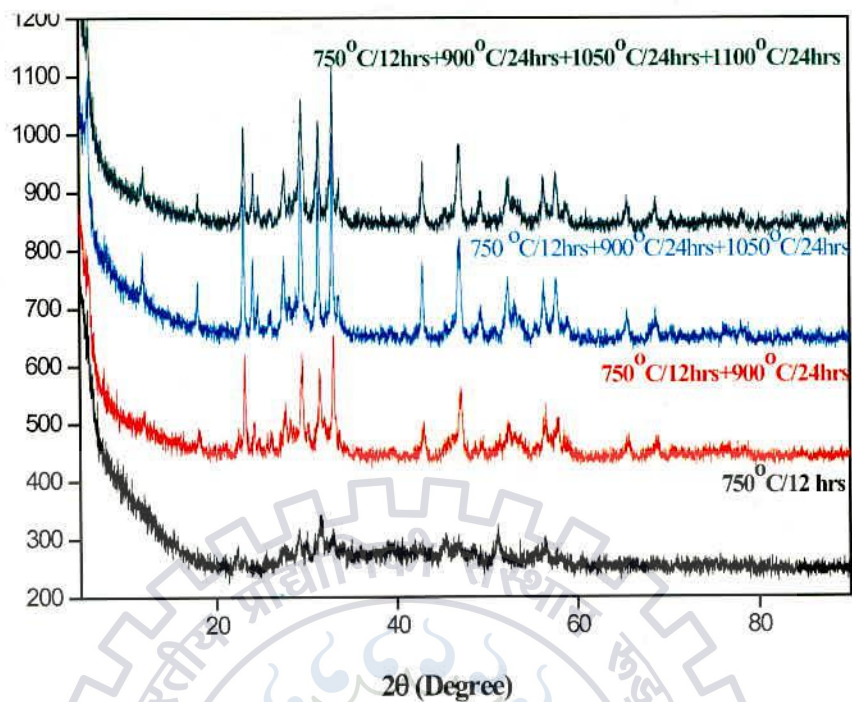
Figure: 4.1: PXD patterns of $KCa_{1.6}La_{0.4}Nb_{2.8}Fe_{0.2}O_{10}$ at different temperatures.

Table 4.2: PXD data for $KCa_{1.6}La_{0.4}Nb_{2.8}Fe_{0.2}O_{10}$.

h	k	l	d_{obs} (Å)	d_{calc} (Å)
0	0	6	4.907	4.915
2	0	0	3.852	3.850
0	0	8	3.688	3.686
2	0	3	3.584	3.585
2	0	4	3.412	3.412
2	0	5	3.223	3.224
2	0	6	3.035	3.030
3	0	7	2.840	2.842
2	2	1	2.710	2.710
2	0	8	2.660	2.662
0	0	14	2.107	2.106
4	0	0	1.925	1.925
2	0	14	1.846	1.848

Refined cell parameter, $a = 7.700(2)$, $c = 29.492(10)$ Å.

38
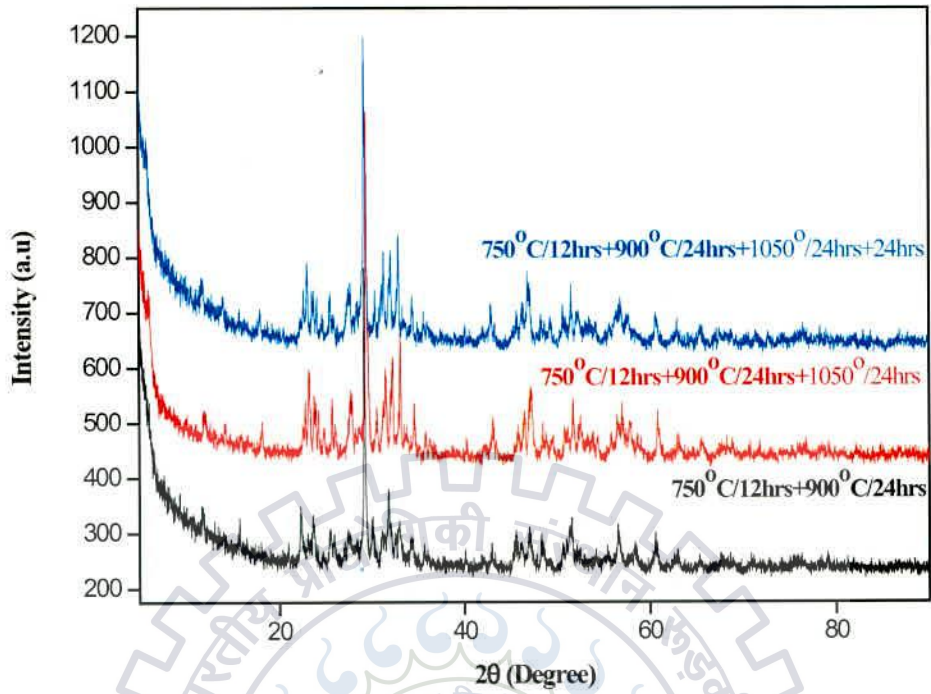
Figure 4.2: PXD patterns of $KCa_{1.6}La_{0.4}Nb_{2.8}Mn_{0.2}O_{10}$ at different temperatures.
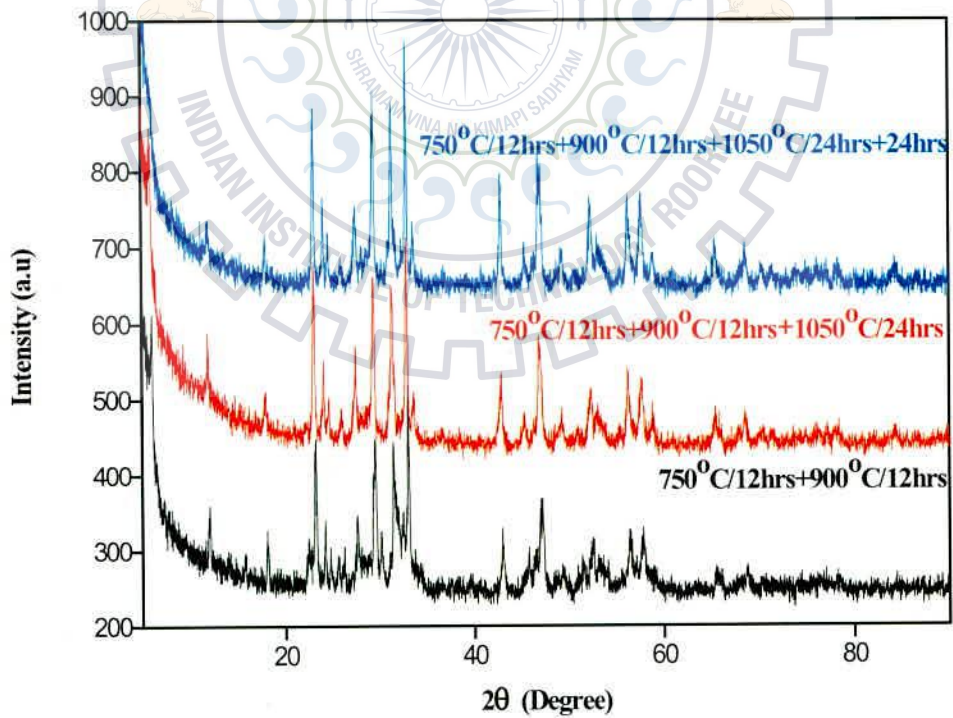
Figure 4.3: PXD patterns of $KCa_{1.6}La_{0.4}Nb_{2.8}Co_{0.2}O_{10}$ at different temperatures.

An analysis of the PXD patterns of $KCa_{1.6}La_{0.4}Nb_{2.8}Mn_{0.2}O_{10}$ and $KCa_{1.6}La_{0.4}Nb_{2.8}Co_{0.2}O_{10}$ with that of JCPDS filed also indicated formation of similar DJ phases. In case of $KCa_{1.6}La_{0.4}Nb_{2.8}Co_{0.2}O_{10}$, the PXD pattern looks very similar to the Fe-analogue. However, for $KCa_{1.6}La_{0.4}Nb_{2.8}Mn_{0.2}O_{10}$, the PXD pattern showed additional reflections that are not present in the parent $KCa_2Nb_3O_{10}$. This could be due to a lower symmetry space group that is adopted by the compound. Further work is required to identify the structure of these compounds.

4.3 FE-SEM and EDX Analysis

The morphology and elemental composition of prepared compounds were analysed by FE-SEM and EDX. Figure 4.4 shows the SEM images of as synthesized $KCa_{1.6}La_{0.4}Nb_{2.8}Fe_{0.2}O_{10}$ at different magnifications (a) 5000×, (b) 10000×, (c) 20000× and (d) 30000×. In all the SEM images homogeneous morphologies of the crystallites are apparent. The plate-like morphologies are characteristic for layered compounds, which are also observed for $KCa_{1.6}La_{0.4}Nb_{2.8}Fe_{0.2}O_{10}$. A representative SEM image (top), its corresponding EDX spectra (middle) and elemental percentages (bottom) for $KCa_{1.6}La_{0.4}Nb_{2.8}Fe_{0.2}O_{10}$ is shown in Figure 4.5. The elemental percentages as obtained from EDX spectrum (bottom panel of Figure 4.5) are in good agreement with the nominal composition of the compound within the allowed experimental error limits.
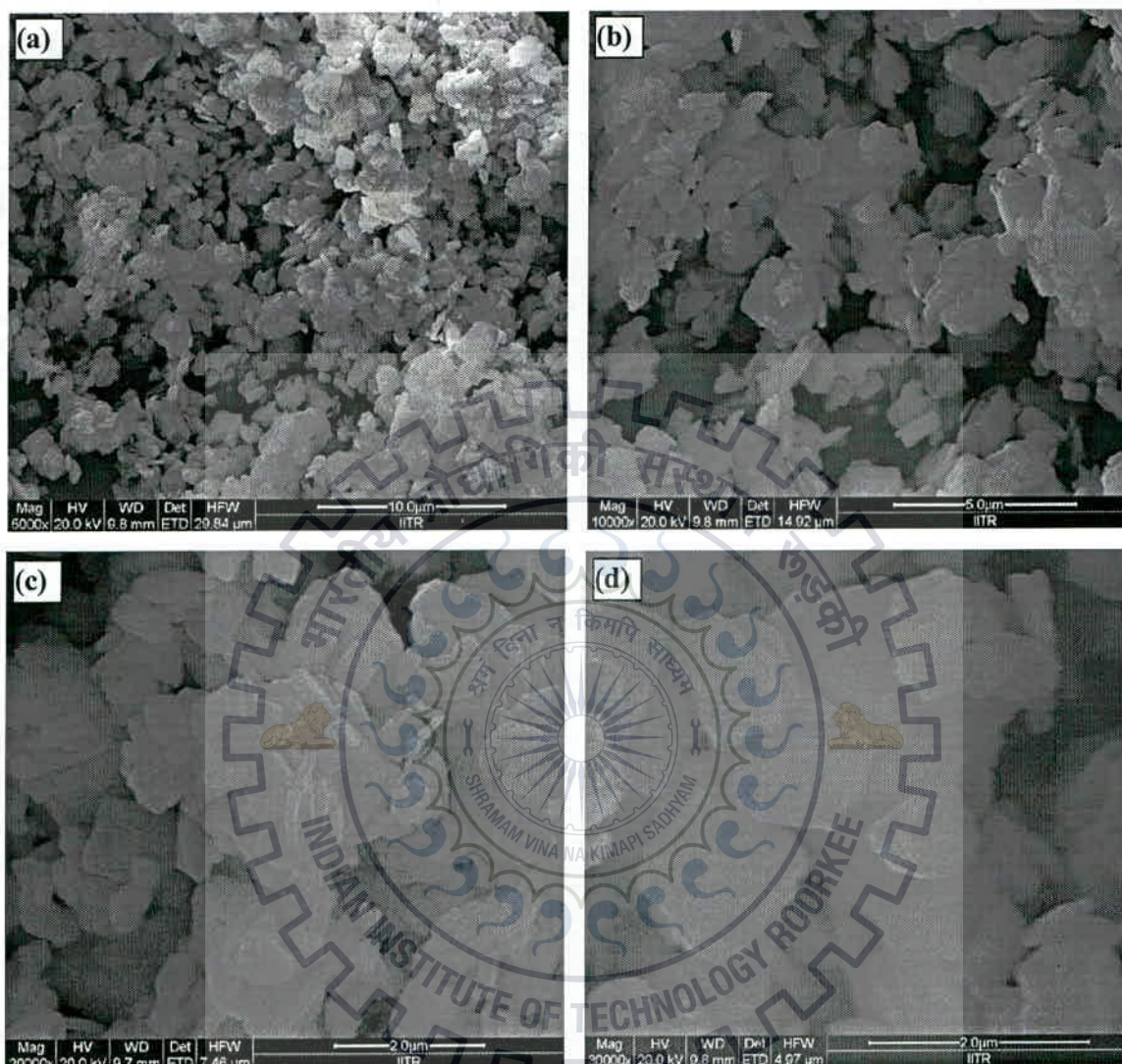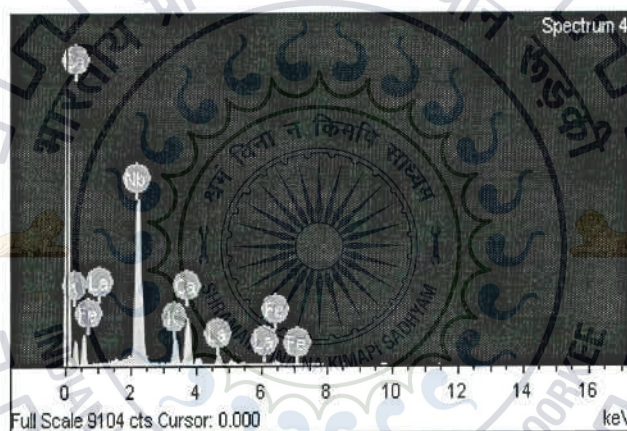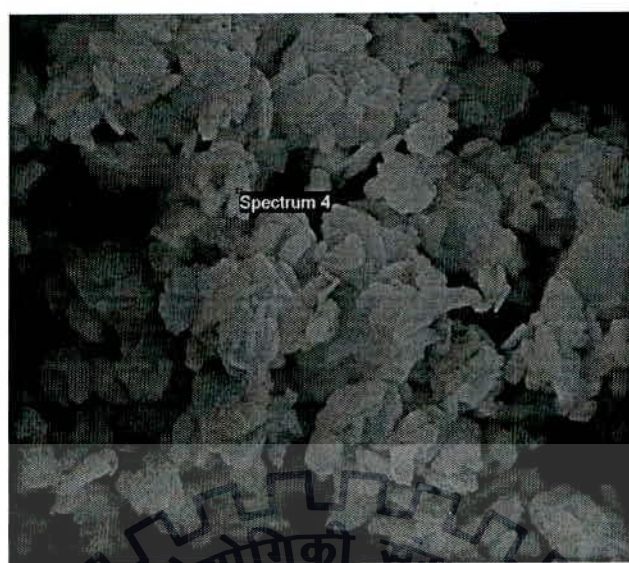
Figure 4.4: SEM images of as synthesized $KCa_{1.6}La_{0.4}Nb_{2.8}Fe_{0.2}O_{10}$ at different magnifications (a) 5000×, (b) 10000×, (c) 20000× and (d) 30000×.

Element	Weight%	Atomic%
K K	7.43	13.88
Ca K	14.30	26.04
Fe K	2.50	3.27
Nb L	65.25	51.28
La L	10.52	5.53

Figure 4.5: SEM image (top), corresponding EDX spectra (middle) and elemental percentages (bottom) for $KCa_{1.6}La_{0.4}Nb_{2.8}Fe_{0.2}O_{10}$.

4.4 UV-Visible Diffuse Reflectance Spectroscopy (UV-Vis DRS)

UV-Vis DRS spectra for $KCa_{1.6}La_{0.4}Nb_{2.8}Fe_{0.2}O_{10}$ is shown in Figure 4.6. The edge absorption is found to be 578.13 nm corresponding to a band gap of 2.15 eV. As compared to the parent compound, $KCa_2Nb_3O_{10}$, which is a UV band gap semiconductor, $KCa_{1.6}La_{0.4}Nb_{2.8}Fe_{0.2}O_{10}$ is a visible band gap semiconductor.
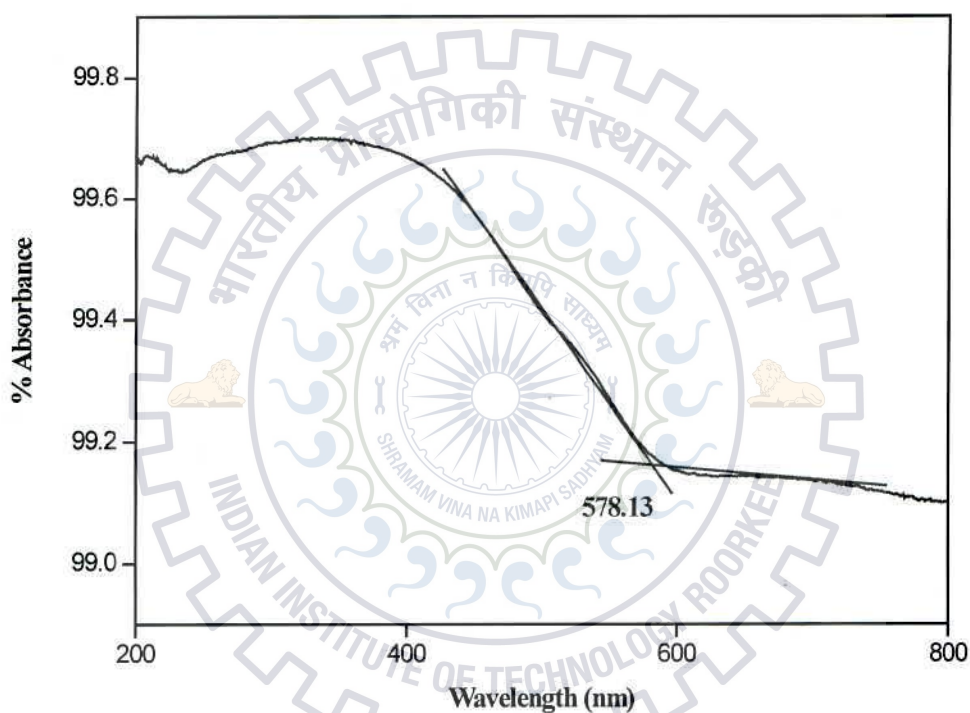

Figure 4.6: UV-Diffuse reflectance spectra of $KCa_{1.6}La_{0.4}Nb_{2.8}Fe_{0.2}O_{10}$

CHAPTER-V

Photocatalytic Activity of Perovskite Titanate, $Pb_{0.5}La_{0.5}Ti_{0.75}Fe_{0.25}O_3$ and Layered Perovskite Niobate, $KCa_{1.6}La_{0.4}Nb_{2.8}Fe_{0.2}O_{10}$

Photocatalytic activity of the prepared compounds was investigated by way of dye degradation test. For this purpose, methylene blue (MB) was chosen as the dye molecule. A 20 ppm solution of MB was used in this study. 100 ml of stock solution was taken in a beaker for degradation test. Natural sunlight was used as irradiation source for photocatalytic reaction.

5.1 Effect of Catalyst Concentration

To know the optimum catalyst concentration for maximum efficiency of degradation of MB, experiments were performed with various amounts of catalyst concentration. The amount of catalysts that were used for the study was, 20, 50, 75 and 100 mg in a fixed volume of the dye solution (10 ml). The solutions with the required amounts of dye were taken in test tubes and each test tube was sonicated for about 15 minutes for well mixing of the catalyst and dye solution and exposed to the natural sunlight. After 2 hours test tubes were centrifuged and the solutions were employed for absorption measurement with a UV-VIS spectrophotometer. The UV-Visible absorption data for $Pb_{0.5}La_{0.5}Ti_{0.75}Fe_{0.25}O_3$ and $KCa_{1.6}La_{0.4}Nb_{2.8}Fe_{0.2}O_{10}$ are shown in Figures 5.1 and 5.2, respectively.
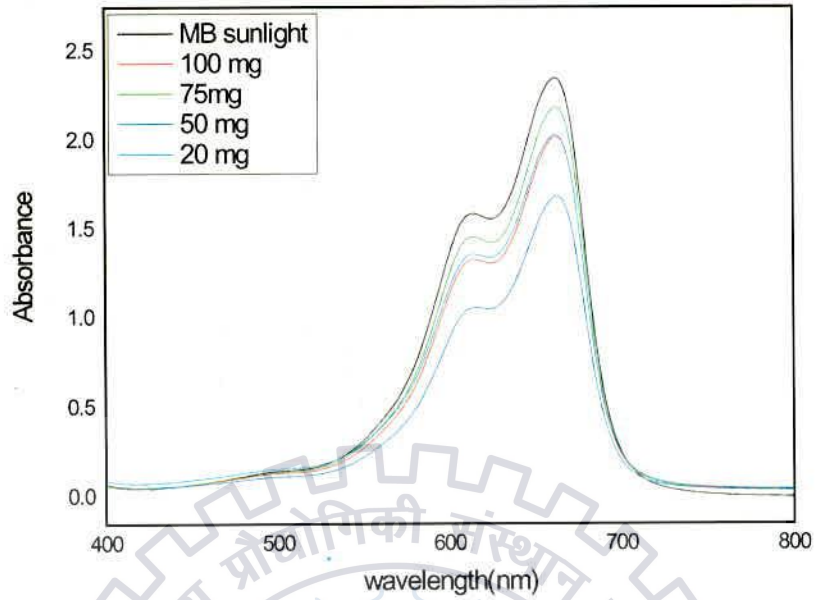
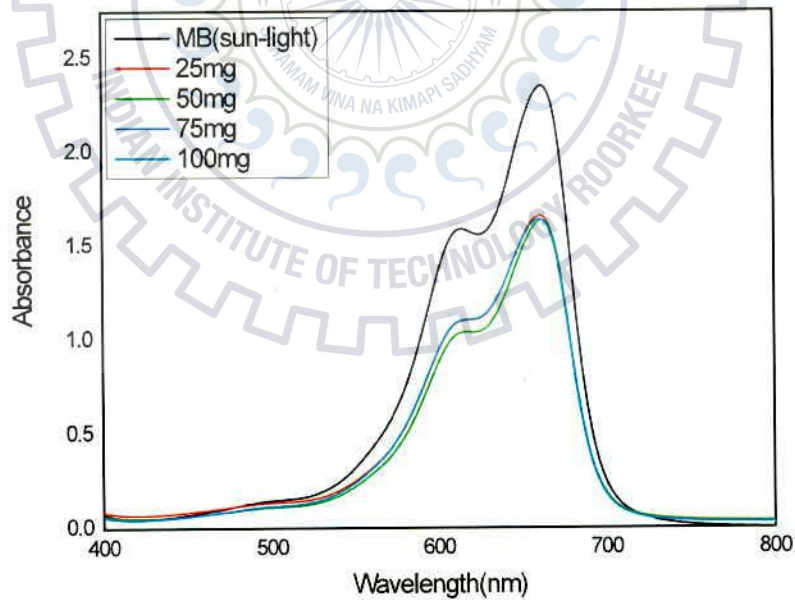**Figure 5.1:** UV-Vis absorbance data for $Pb_{0.5}La_{0.5}Ti_{0.75}Fe_{0.25}O_3$ with MB after 2 hours of solar irradiation.

Figure 5.2: UV-Vis absorbance data for $KCa_{1.6}La_{0.4}Nb_{2.8}Fe_{0.2}O_{10}$ with MB after 2 hours of solar irradiation.

The absorption data recorded at the characteristics peak of MB at 664 nm shows that both the catalyst is active towards photocatalytic degradation of MB. From Figure 5.1 it is evident that maximum degradation of MB is taking place with 50 mg/10 ml catalyst concentration, since absorption maximum is decreased significantly for this concentration as compared to that for three other concentrations. This may be due to the maximum exposure of the catalyst for adsorption and active sites on the surface of the catalyst. This is the optimum concentration for the degradation of 20 ppm of MB by the titanate perovskite. Decrease in activity of the catalyst at higher concentration could be due to the "shielding effect" which is caused by suspended catalyst layer located closer to the radiation sources and agglomeration of catalyst particles at the higher level of catalyst amount [46]. In case of $KCa_{1.6}La_{0.4}Nb_{2.8}Fe_{0.2}O_{10}$ only a very little effect of concentration on the degradation of 20 ppm MB dye solution is observed (Figure 5.2).

5.2 Effect of Irradiation Time

The effect of irradiance time on photocatalytic degradation of MB from its aqueous solution was investigated under natural sunlight with the optimum catalyst concentration as obtained from the previous experiment. The degree of photodegradation as a function of time was studied for both $Pb_{0.5}La_{0.5}Ti_{0.75}Fe_{0.25}O_3$ and $KCa_{1.6}La_{0.4}Nb_{2.8}Fe_{0.2}O_{10}$.

For time dependant study 100 ml of 10 ppm MB solution were prepared in Millipore water. For titanate perovskite 500 mg of catalyst were dissolved in 100 ml of 10 ppm MB solution. After that, the solution was kept under magnetic stirring condition for one hour in the dark to ensure maximum adsorption of dye on catalyst surface. After one hour, the beaker was taken out and kept under solar radiation. At every 10 minutes interval, 5 ml of the solution were

taken and centrifuged and UV-Visible spectra were recorded. Figure 5.3 shows the changes in the absorption of MB dye as a function of time for $Pb_{0.5}La_{0.5}Ti_{0.75}Fe_{0.25}O_3$.
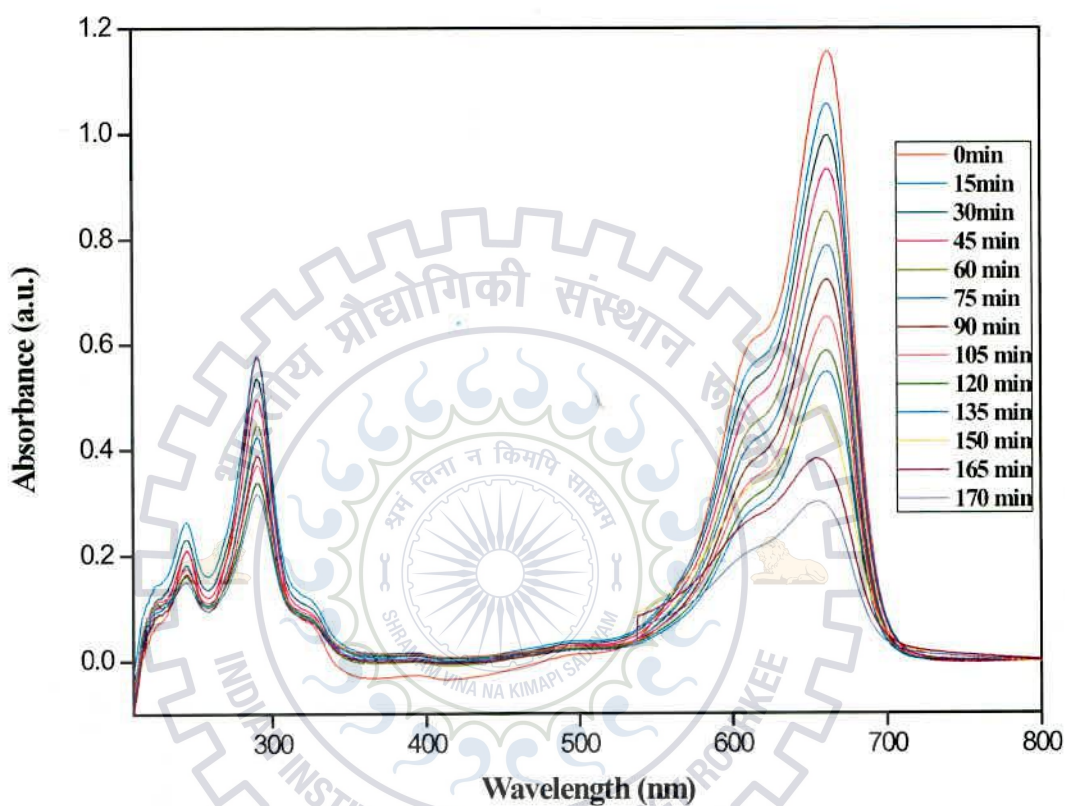

Figure 5.3: Changes in the UV-Vis absorption of MB (10 ppm) with time for $Pb_{0.5}La_{0.5}Ti_{0.75}Fe_{0.25}O_3$.

It has been found that 80 % degradation of the MB dye takes place in 170 minutes under the solar radiation. For complete degradation studies further works has to be carried out with longer durations or under stirring conditions. Because, with time the catalyst might settle and will no more be dispersed for effective degradation.

47

For the time dependant study of dye degradation by $KCa_{1.6}La_{0.4}Nb_{2.8}Fe_{0.2}O_{10}$, 100 ml of 20 ppm MB solution were prepared in Millipore water. For degradation study, 500 mg of the compound were dissolved in 100 ml of 20 ppm MB solution. Figure 5.4 shows the changes in the absorption of MB dye as a function of time for $KCa_{1.6}La_{0.4}Nb_{2.8}Fe_{0.2}O_{10}$. It has been found that 92 % degradation of the MB dye takes place in 240 minutes under the solar radiation. However, the self degradation of the dye after same amount of solar irradiation was 29% (Figure 5.5). This, in fact, confirms the photocatalytic activity of the prepared perovskite titanate and the layered perovskite niobate. The MB dye degradation data for $KCa_{1.6}La_{0.4}Nb_{2.8}Fe_{0.2}O_{10}$ is also shown as a function of time in Figure 5.6.
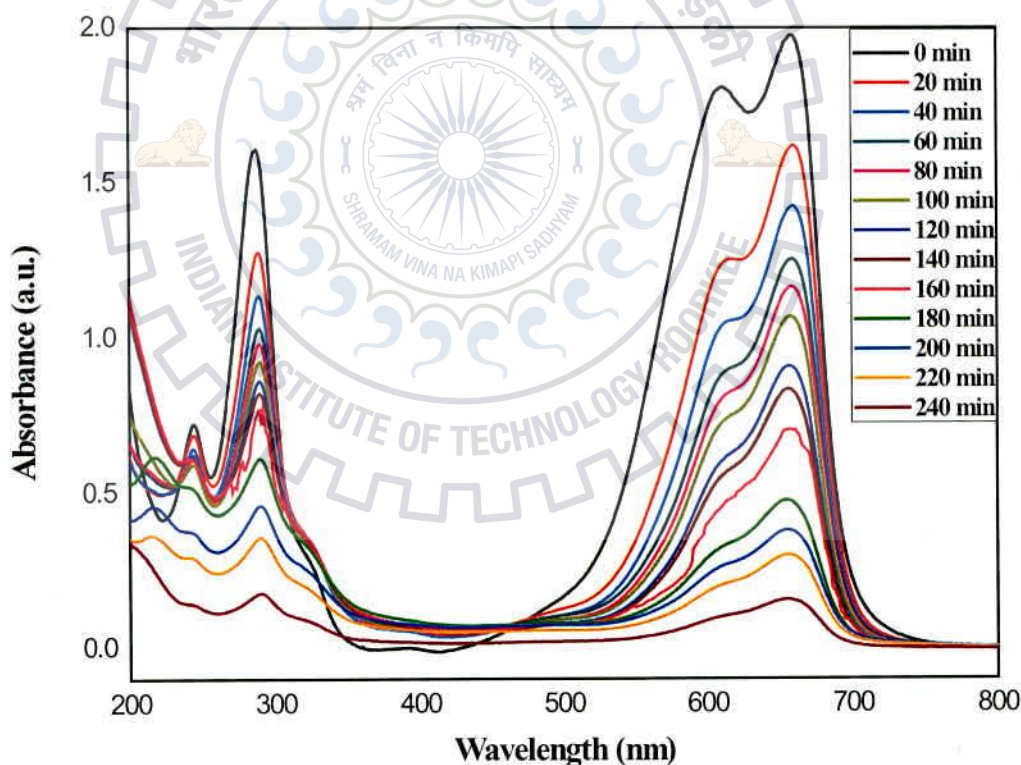

Figure 5.4: Changes in the UV-Vis absorption of MB (20 ppm) with time for
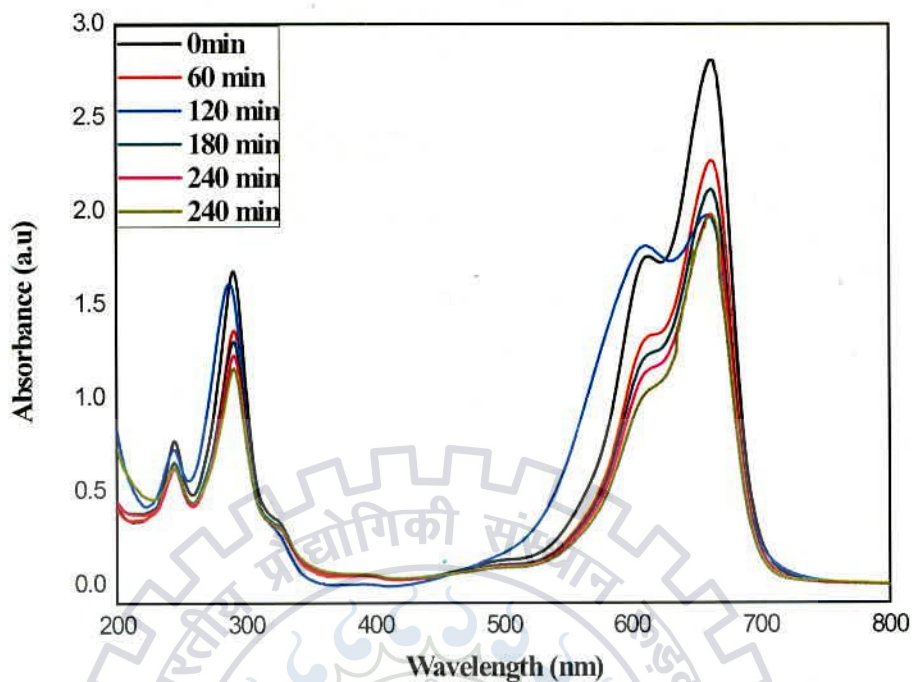$KCa_{1.6}La_{0.4}Nb_{2.8}Fe_{0.2}O_{10}$.

48

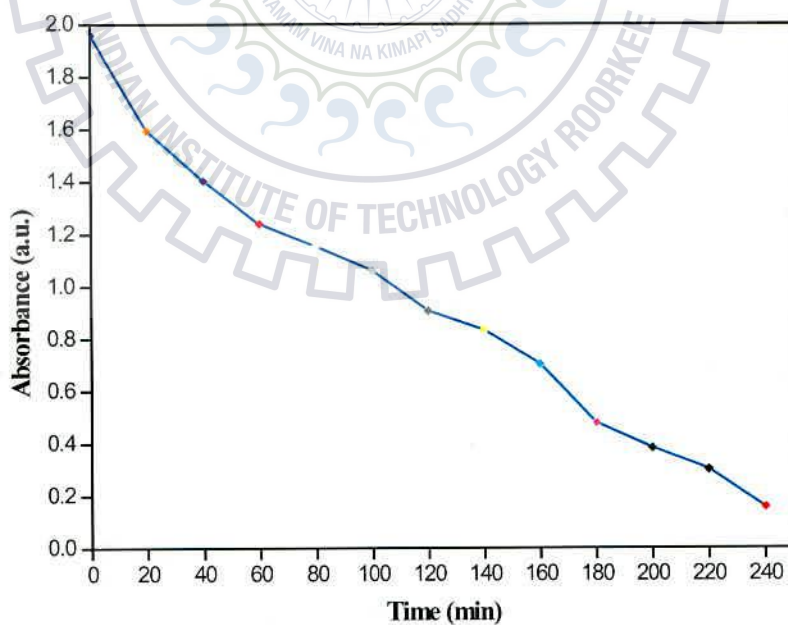**Figure 5.5: Changes in the UV-Vis absorption of MB (20 ppm) with time due to self-degradation.**

Figure 5.6: Absorption maximum of MB with time for $KCa_{1.6}La_{0.4}Nb_{2.8}Fe_{0.2}O_{10}$.

Figure 5.7 shows a comparison of MB degradation in presence of $KCa_{1.6}La_{0.4}Nb_{2.8}Fe_{0.2}O_{10}$ in comparison with its self-degradation studies. Further works are necessary to fully explore the potential of these photocatalysts. It will be interesting to compare and correlate the photocatalytic activities of all the synthesized compounds in a future study.
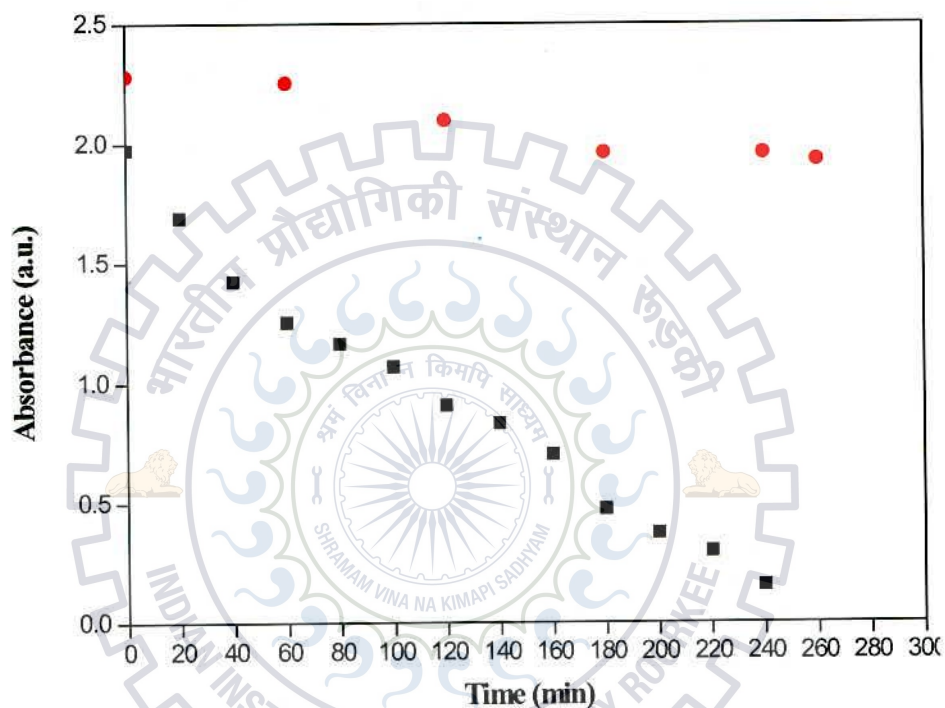

Figure 5.7: Absorbance data of MB for $KCa_{1.6}La_{0.4}Nb_{2.8}Fe_{0.2}O_{10}$ in comparison with self-degradation.

References

[1]. Fujishima, K.; Honda, K., *Nature*, **1972**, *238*, 37.

[2]. Heller, A., *Acc. Chem. Res.*, **1995**, *28*, 503.

[3]. Linsebigler, A.; Lu, G.; Yates, J. T., *Chem. Rev.*, **1995**, *95*, 735.

[4]. Hadjiivanov, K. I.; Klissurski, D. K., *Chem. Soc. Rev.,* **1996**, *25*, 61.

[5]. Asahi, R.; Morikawa, T.; Ohwaki, T.; Aoki, K.; Taga, Y., *Science*, **2001,** *293*, 269.

[6]. Osterloh, F. E., *Chem. Mater.*, **2008**, *20*, 35.

[7]. Kudo, A.; Miseki, Y., *Chem. Soc. Rev.*, **2009**, *38*, 253.

[8]. Chen, X.; Shen, S.; Guo, L.; Mao, S. S., *Chem. Rev.*, **2010**, *110*, 6503.

[9]. Maeda, K.; Domen, K., *J. Phys. Chem. Lett.*, **2010**, *1*, 2655.

[10]. Fox, M. A.; Dulay, M. T.; *Chem. Rev.*, **1993**, *93*, 341.

[11]. Hoffman, M. R.; *Chem. Rev.*, **1995**, *95*, 69.

[12]. Yoshimura, J.; Ebina, Y.; Kondo, J.; Domen, K.; Tanaka, A., *J. Phys. Chem.*, **1993**, *97*, 1970.

[13]. Kim, H. G.; Hwang, D. W.; Lee, J. S., *J. Am. Chem. Soc.*, **2004**, *126*, 8912.

[14]. Tang, J.; Zou, Z.; Ye, J., *Angew. Chem. Int. Ed.*, **2004**, *43*, 4463.

[15]. Fu, H.; Pan, C.; Yao, W.; Zhu, Y., *J. Phys. Chem. B*, **2005**, *109*, 22432.

[16]. Shimodaira, Y.; Kato, H.; Kobayashi, H.; Kudo, A., *J. Phys. Chem. B*, **2006**, *110*, 17790.

[17]. Wang, D.; Kako, T.; Ye, J., *J. Am. Chem. Soc.*, **2008**, *130*, 2724.

[18]. Hosogi, Y.; Kato, H.; Kudo, A., *J. Phys. Chem. C*, **2008**, *112*, 17678.

[19]. Kim, H. G.; Borse, P. H.; Jang, J. S.; Ahn, C. W.; Jeong, E. D.; Lee, J. S., *Adv. Mater.*, **2011**, *23*, 2088.

[20]. Ungelenk, J.; Feldmann, C., *Chem. Commun.*, **2012**, *48*, 7838.

[21]. Huang, L.; Chu, S.; Wang, J.; Kong, F.; Luo, L.; Wang, Y.; Zou, Z., *Catal. Today*, (2012), http://dx.doi.org/10.1016/j.cattod.2012.08.026.

[22]. Andreozzi, R.; Caprio,V.; Insola, A.; Marotta, R., *Catalysis Today*, **1999**, *53*, 51.

[23]. Paola, A. D.; Garcia-Lopez, E.; Merci, G.; Palmisano, L., *J. Hazard. Mater.*, **2012**, 211-212, 3.

[24]. Konstantinou, I. K.; Albanis, T. A., *Applied Catalysis B: Environmental*, **2003**, *42*, 319.

[25]. Shiragami, T.; Fukami, S.; Wada, Y.; Yanagida, S., *J. Phys. Chem.*, **1993**, *97*, 12882.

[26]. Machida, M.; Murakami, S.; Kijima, T., *J. Phys. Chem. B*, **2001**, *105*, 3289.

[27]. Kar, A.; Kundu, S.; Patra, A., *RSC Advances*, **2012**, *2*, 10222.

[28]. Frank, S. N.; Bard, A. J., *J. Am. Chem. Soc.*, **1977**, *99* 304.

[29]. Kumar, S. G.; Devi, L. G., *J. Phys. Chem. A*, **2011**, *115*, 13211.

[30]. Conronado, J. M.; Maira, A. J.; Conesa, J. C.; Yeung, K. L.; Augugliaro, V.; Soria, J., *Langmuir*, **2001**, *17*, 5368.

[31]. Mitchell, R. H., *Perovskites: Modern and Ancient*; Almaz Press: Thunder Bay, Canada. (**2002**).

[32]. Aurivillius, B., *Ark. Kemi*, **1949**, *1*, 463; Aurivillius, B., *Ark. Kemi*, **1950**, *2*, 519.

[33]. Ruddlesden, S. N.; Popper, P., *Acta. Crystallogr.*, **1957**, *10*, 538; Ruddlesden, S. N.; Popper, P., *Acta. Crystallogr.*, **1958**, *11*, 54.

[34]. Dion, M.; Ganne, M.; Tournoux, M., *Mater. Res. Bull.*, **1981**, *16*, 1429; Jacobson, A. J.; Johnson, J. W.; Lewandowski, J. T., *Inorg. Chem.*, **1985**, *24*, 3727.

[35]. Ishihara, T.; Nishiguchi, H.; Fukamachi, K.; Takita, Y., *J. Phys. Chem. B*, **1999**, *103*, 1.

[36]. Kasahara, A.; Nukumizu, K.; Hitoki, G.; Takata, T.; Kondo, J. N.; Hara, M.; Kobayashi, H.; Domen, K., *J. Phys. Chem. A*, **2002**, *106*, 6750.

[37]. Fei, D. Q.; Hudaya, T. Adesina, A. A., *Catal. Commun.*, **2005**, *6*, 253.

[38]. Xu, X.; Randorn, C.; Efstathiou, P.; Irvine, T. S., *Nature Materials*, **2012**, *11*, 595.

[39]. Subramanian, M. A.; Gopalakrishnan, J.; Sleight, A. W., *Mater. Res. Bull.*, **1988**, *23*, 837.

[40]. Mitsuyama, T.; Tsutsumi, A.; Sato, S.; Ikeue, K.; Machida, M., *J. Solid State Chem.*, **2008**, *181*, 1419.

[41]. Choi, W. S.; Chisholm, M. F.; Singh, D. J.; Choi, T.; Jellison Jr, G. E.; Lee, H. N., *Nature Commun.*, **2012**, *3*, 689.

[42]. Losocha, W.; Lewinski, K., *J. Appl. Crystallogr.*, **1994**, *27*, 437.

[43]. Kraus, W.; Nolze, G., *Powder Cell 2.4*, free software available at http://www.ccp14.ac.uk.

[44]. Shapiro, I. P., *Opt. Spektrosk.*, **1958**, *4*, 256.

[45]. Eng, H. W.; Barnes, P. W.; Auer, B. M.; Woodward, P. M., *J. Solid State Chem.*, **2003**, *96*, 535.

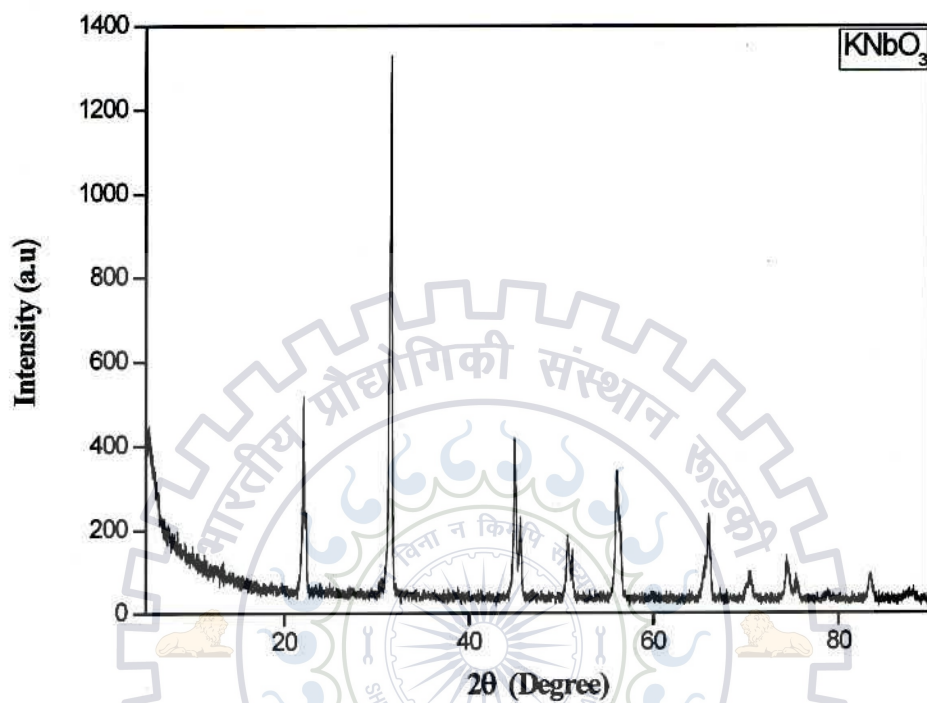[46]. Wang, H.-L.; Zhao, D.-Y.; Jiang, W.-F., *Desalination and Water Treatment*, **2013**, *51*, 2826.

Appendix

Figure A1: PXD pattern of KNbO₃.